J. Fluid Mech. (2010), *vol.* 648, *pp.* 435–469.
doi:10.1017/S0022112009992758

Disturbance evolution in a Mach 4.8 boundary layer with two-dimensional roughness-induced separation and shock

OLAF MARXEN†, GIANLUCA IACCARINO AND ERIC S. G. SHAQFEH

Center for Turbulence Research, Building 500, Stanford University, Stanford, CA 94305-3035, USA

(Received 21 April 2009; revised 12 October 2009; accepted 13 October 2009)

A numerical investigation of the disturbance amplification in a Mach 4.8 flat-plate boundary layer with a localized two-dimensional roughness element is presented. The height of the roughness is varied and reaches up to approximately 70 % of the boundary-layer thickness. Simulations are based on a time-accurate integration of the compressible Navier–Stokes equations, with a small disturbance of fixed frequency being triggered via blowing and suction upstream of the roughness element. The roughness element considerably alters the instability of the boundary layer, leading to increased amplification or damping of a modal wave depending on the frequency range. The roughness is also the source of an additional perturbation. Even though this additional mode is stable, the interaction with the unstable mode in the form of constructive and destructive interference behind the roughness element leads to a beating and therefore transiently increased disturbance amplitude. Far downstream of the roughness, the amplification rate of a flat-plate boundary layer is recovered. Overall, the two-dimensional roughness element behaves as disturbance amplifier with a limited bandwidth capable of filtering a range of frequencies and strongly amplifying only a selected range.

1. Introduction

The prediction of heat loads on the surface of vehicles (re-)entering a planetary atmosphere is important for heat-shield design. Turbulent flow induces much higher heating in comparison to laminar flow. Therefore, the prediction of the occurrence of laminar–turbulent transition is a key factor in defining the dimensions and materials used for the thermal protection system. Yet, fundamental physical processes related to laminar–turbulent transition in high-speed boundary layers are not well understood. This is true even for the first stages of the process, that is, generation and amplification of small-amplitude (or linear) perturbations, to which this article is restricted. High-speed boundary layers may exhibit qualitatively different phenomena than incompressible ones. Among these are shocklets and multiple instability mechanisms as well as disturbance–generation mechanisms, all of which influence the disturbance evolution.

† Email address for correspondence: olaf.marxen@stanford.edu

1.1. *The unstable discrete mode(s)*

1.1.1. *Inviscid flow*

Mack (1969, 1975) considered the linear instability of high-speed flat-plate boundary layers theoretically. Using, at first, inviscid linear stability theory (inviscid LST) he found several instability mechanisms. The most important ones are an instability caused by a generalized inflection point in the boundary-layer profile and an instability caused by an acoustic wave being trapped inside the boundary layer. The former type of instability also exists in incompressible flow and has been labelled 'first-mode' instability by Mack (1969). The latter type of instability has no incompressible counterpart, as it is due to a region of locally supersonic flow relative to the phase velocity of the disturbance wave. This type of instability is commonly denoted as 'second-mode' or 'Mack mode' instability. Analogous to the second-mode type of instability, there exist higher inviscid instability modes ('third', 'fourth' or just 'higher Mack modes'), but these are usually not considered important in practice due to small amplification rates.

1.1.2. *Viscous flow*

According to Mack (1969), the similarities between viscous and inviscid flow are sufficiently strong so that he kept the same terminology. However, Tumin (2007) pointed out that for viscous flow at finite Reynolds numbers, only one unstable mode may be present, and Mack (1969)'s classification of (two different) modes as applied to the viscous flow may therefore not be appropriate. In viscous LST (hereafter LST) for the spatial problem (real frequency, complex streamwise wavenumber), the unstable mode is represented by a pole that moves in the complex plane with variation in frequency or Reynolds number (Tumin 2007). Depending on these two parameters, regions exist where the modal disturbance exhibits characteristics of the inviscid 'first-mode instability' or 'second-mode instability'. For flat plates, these regions occur consecutively for increasing frequency or streamwise Reynolds number: the region of first-type characteristic is followed by the region of second-type characteristic, which is followed by the region of third-type characteristic, and so forth.

As the terminology 'first mode' and 'second mode' is still widely used in the high-speed transition community, here we will refer to these mode characteristics by the 'first-type' and 'second-type' instabilities, respectively. Note also that the driving physical mechanism behind the instability is different in different frequency and Reynolds number regimes, while at the same time it is made clear that there are not two different modes. Unlike in incompressible flow, the largest growth rates occur for non-zero spanwise wavenumbers if the instability mode possesses 'first-type' characteristics. If it exhibits 'second-type' characteristics, the most-amplified wave is two-dimensional. Pagella, Rist & Wagner (2002) showed that the growth of a two-dimensional unstable mode in the first-type region for a flat plate is underpredicted by LST due to non-parallel effects.

1.2. *The stable discrete modes*

Beside the instability mode, other, though stable, discrete modes play a role in the evolution of perturbations inside the boundary layer. These modes were described by Mack (1969) and were denoted as 'multiple viscous solution' (MVS). Several of these stable modes exist: for each of the different characteristic regions of the unstable mode, a stable mode exists (see for instance figure 7 of Ma & Zhong 2003*a*). The locations where the respective stable and unstable modes have the same phase

velocities are usually the locations that separate the characteristic regions of the unstable mode.

Fedorov (2003) discussed that at small Reynolds numbers one discrete mode is synchronized with the slow acoustic (free-stream) mode (see § 1.3), whereas another mode is synchronized with the fast acoustic mode. Therefore, he suggested calling these discrete modes slow and fast discrete modes, respectively. For instance, in an example by Tumin (2007) at Mach 5.6, the unstable mode is the slow discrete mode while the fast discrete mode is a stable mode. On the other hand, more than one stable mode exists, and these may all arise from the fast acoustic mode (again, see figure 7 of Ma & Zhong 2003*a*), making such a denotation not unique. Moreover, just as Mack (1969)'s description of the different inviscid instability modes – reminiscent of an infinitely large Reynolds number, Re – is not necessarily a good choice for finite Reynolds number as argued by Tumin (2007), a description based on Re approaching zero might not be helpful either. For boundary layers that are not self-similar, a straightforward tracking of poles for Re going to zero or to infinity is not possible.

For these reasons, we will later call the discrete mode that can become unstable 'the instability mode', with 'first-type' or 'second-type' characteristics, even though it is understood that for certain frequencies and Reynolds numbers, this mode may be stable. The stable modes, on the other hand, will be denoted so as to emphasize that they separate regions of first-, second- and higher-type instability characteristics: 'stable mode 1–2', 'stable mode 2–3', and so forth.

In numerical simulations, Eissler & Bestek (1996) observed that blowing and suction at the wall in the region of first-type instability can excite such a stable mode. Moreover, they showed that the superposition of the unstable and the stable modes can lead to a beating in the wall-pressure signal via a constructive and destructive interference. Such an interference is possible since the stable mode often possesses a similar amplitude function close to the wall as the unstable mode, in particular in the region of first-type instability characteristics.

1.3. *The continuous spectra*

Apart from the discrete modes, there exist several continuous spectra in the solution of the spatial linear stability problem (Schmid & Henningson 2001). For compressible flat-plate boundary layers, seven of them can be found (see for instance discussion in Balakumar & Malik 1992), of which four correspond to the downstream disturbance evolution. The remaining three possess large decay rates and therefore the upstream influence from a localized disturbance is small (Balakumar & Malik 1992). The four branches relevant for downstream disturbance evolution correspond to fast acoustic modes, slow acoustic modes, vorticity modes and entropy modes.

Tumin (2007) showed that the vorticity and entropy modes do not penetrate the boundary layer. More precisely, eigenfunctions for the vorticity and the entropy mode possess oscillations that are wave solutions in the free stream. However, despite the oscillations, Tumin (2006) pointed out that the sum of these modes can result in zero perturbations above the Mach wave. For three-dimensional roughness elements, a superposition of modes from the continuous spectrum can represent streamwise vortices localized inside the boundary layer behind the roughness (Tumin & Reshotko 2005; Tumin 2006). For two-dimensional roughness elements considered in this paper, however, we assume that the vorticity and entropy modes are not relevant. The acoustic modes, which have significantly larger velocity perturbations close to the wall than outside the boundary layer, may play a role in cases with two-dimensional roughness.

1.4. *Receptivity, modal interactions and conversion of modes*

For a flat plate in supersonic flow, the stage of disturbance generation near the plate's leading edge has been studied by Ma & Zhong (2003*a*) numerically and compared with theoretical results. In particular, they focused on the origin of instability waves in the second-type instability region. Ma & Zhong (2003*a*) argue that '... resonant (synchronization) interactions [of stable modes] with both acoustic waves and the Mack-mode waves' (p. 31) occur. According to Ma & Zhong (2003*a*), 'the stable wave modes ... are critical in transferring wave energy between the acoustic waves and the unstable second mode.' (p. 31). Similarly, Eissler & Bestek (1996) suggested that 'The discrepancies [between LST and numerical simulation as they observed] for the two-dimensional amplitudes ... might be the result of an exchange between the two modes as described recently by Fedorov & Khokhlov (1993).' Tumin (2007), following Fedorov & Khokhlov (2001), summarizes this as a route to transition: 'vorticity/entropy modes → decaying discrete mode → unstable discrete mode → transition to turbulence'. To provide sufficient evidence for this route, Tumin (2007) suggested applying a method based on a multi-mode decomposition of DNS data in order to evaluate the amplitude of the decaying modes (Tumin, Wang & Zhong 2007). However, the existence of this route currently remains an open question. Moreover, it is not yet clear how differences between LST eigenfunction and amplitude functions from numerical simulations due to non-parallel effects impact the multi-mode decomposition. For these reasons, it is desirable to find ways to interpret simulation results alone in order to supplement these theoretical tools. A viable way, which will be employed here, is a variation of the dimensions of the disturbance strip, followed by a comparison of respective results.

Balakumar (2003) investigated the steady flow field induced by two- and three-dimensional roughness at Mach 3.5. Moreover, he investigated the receptivity process regarding the interaction of a roughness with an acoustic wave and found that the roughness plays only a minor role in generating boundary-layer perturbations.

1.5. *Disturbance evolution in separated boundary layers*

At present, many physics-based transition prediction methods rely on the LST by applying the e^N-method; see for example Malik (1989, 2003). Because of a limited knowledge of processes involving disturbance generation and nonlinear stages of disturbance evolution, the prediction is currently not very accurate even for smooth surfaces. However, the situation is even worse if abrupt geometrical changes caused, for instance, by steps or ramps occur and result in boundary-layer separation. For these cases, even the linear amplification may no longer be predicted accurately due to significant non-parallel effects.

From studies of a weak shock impinging on a boundary layer (Pagella *et al.* 2002) or a compression-ramp flow (Pagella, Babucke & Rist 2004), it is known that regions of boundary-layer separation may considerably increase convective amplification with second-type characteristics. Both Pagella *et al.* (2002) and Pagella *et al.* (2004) argued that non-parallel effects are responsible for most of the deviations seen between LST and numerical simulations. A comparison of local LST with results from numerical simulations in Pagella *et al.* (2002, 2004) for separating flow was restricted to second-type waves, and an assessment of the accuracy of LST for first-type (two-dimensional and oblique) waves in separating flow is still lacking. This article addresses this issue and includes a more complete comparison.

Even though many practical applications possess three-dimensional rather than two-dimensional roughness elements, the latter type of element may be seen as

the limiting case for an increasingly close spacing of three-dimensional roughness elements. Also, it may be considered representative for flows with boundary-layer separation due to geometrical changes.

At least three fundamentally different types of physical mechanisms may influence disturbance evolution. First, the disturbance amplitude may be increased due to a (convective) amplification boost. Such a boost should be caused by a stronger instability due to boundary-layer separation. This mechanism can best be investigated in the region upstream of the roughness, where the local geometry is still that of a flat plate and the flow is only affected by the roughness-induced pressure gradient. It is in this region where we will carry out the detailed comparison between LST and numerical simulation.

Second, the roughness may become a source of additional boundary-layer perturbations that are absent on smooth surfaces. Even though the roughness is stationary (unlike the blowing and suction slot of Eissler & Bestek 1996), it may (indirectly) act as an oscillator. Note that the roughness itself may not necessarily be the source but might induce flow features absent without the roughness, such as shocks, responsible for the new disturbance generation. This mechanism will be studied in the region behind the roughness.

Third, transition to a state of large-amplitude unsteadiness may occur immediately in front or behind the roughness, due to an absolute instability of the separation zone – even in the absence of oncoming disturbances. Such a mechanism has been studied by Robinet (2007) in the case of shock–boundary-layer interaction. Such a study is beyond the scope of this article. For the cases considered here, we did not observe any appearance of unforced disturbances that would suggest the presence of an absolute or global instability.

1.6. *Outline*

The paper is structured as follows. First, the governing equations for numerical simulations are given. This section includes a description of the numerical method, together with the boundary conditions and the roughness geometry (§ 2). Results from numerical simulation regarding the steady-state base flow (§ 3) and the disturbed flow (§ 4) are discussed in order to evaluate physical mechanisms leading to disturbance growth. Findings are summarized in § 5.

2. Governing equations, numerical method and geometry

2.1. *Governing equations*

The governing equations are the time-dependent three-dimensional Navier–Stokes equations for a compressible fluid in non-dimensional form. These equations are formulated for a calorically perfect gases with density ρ, temperature T and pressure p. Non-dimensionalization is mostly based on the free-stream conditions (marked by $_\infty$): a reference temperature $\tilde{T}_{ref} = (\gamma - 1)\tilde{T}_\infty$, density $\tilde{\rho}_\infty$, specific heat ratio $\gamma = \tilde{c}_p/\tilde{c}_v$, the speed of sound $\tilde{c}_\infty$, thermal conductivity $\tilde{k}_\infty$, viscosity $\tilde{\mu}_\infty$ and a reference length $\tilde{L}_{ref}$ (all dimensional quantities are marked by $\tilde{}$). The velocity vector is given by $[u_1\, u_2\, u_3]^{\mathrm{T}} = [u\, v\, w]^{\mathrm{T}}$. It is a function of all three spatial dimensions $[x_1\, x_2\, x_3]^{\mathrm{T}} = [x\, y\, z]^{\mathrm{T}}$ and time t. This results in the following set of equations for mass, momentum and energy conservation:

$$\frac{\partial \rho}{\partial t} + \frac{\partial}{\partial x_j}(\rho u_j) = 0, \tag{2.1}$$

$(Re_\infty\, M_\infty)$	Pr_∞	M_∞	T_S	x_1	x_2	y_1	y_2	NX	MY	LP	s_R	$x_{c,R}$	γ
10^5	0.71	4.8	1.993	1.6065	44.4465	see (2.13)	1.575	1200	200	600	20.0	15.0	1.4

TABLE 1. Simulation parameters for two-dimensional simulations.

$$\frac{\partial \rho u_i}{\partial t} + \frac{\partial}{\partial x_j}(\rho u_i u_j + p\delta_{ij}) = \frac{\partial \sigma_{ij}}{\partial x_j}, \quad i = 1, 2, 3, \tag{2.2}$$

$$\frac{\partial E}{\partial t} + \frac{\partial}{\partial x_j}[(E + p)u_j] = -\frac{\partial q_j}{\partial x_j} + \frac{\partial}{\partial x_k}(u_j \sigma_{jk}). \tag{2.3}$$

The total energy per unit mass E, the viscous stress tensor σ_{ij} and the heat flux vector q_j are defined as (note that the temperature and velocity scales are $(\gamma - 1)\tilde{T}_\infty$ and $\tilde{c}_\infty$, respectively):

$$E = e\rho + \tfrac{1}{2}\rho u_i u_i, \tag{2.4}$$

$$\sigma_{ij} = \frac{\mu}{Re_\infty}\left(\frac{\partial u_i}{\partial x_j} + \frac{\partial u_j}{\partial x_i} - \frac{2}{3}\frac{\partial u_k}{\partial x_k}\delta_{ij}\right), \tag{2.5}$$

$$q_i = \frac{-1}{Re_\infty Pr_\infty} k_e \frac{\partial T}{\partial x_i}. \tag{2.6}$$

The Reynolds number Re_∞ and the Prandtl number Pr_∞ are

$$Re_\infty = \tilde{\rho}_\infty \tilde{c}_\infty \tilde{L}_{ref}/\tilde{\mu}_\infty, \tag{2.7}$$

$$Pr_\infty = \tilde{\mu}_\infty \tilde{c}_p/\tilde{k}_\infty\,. \tag{2.8}$$

The Mach number M_∞ is computed with the streamwise velocity in the free-stream $\tilde{u}_\infty$ and the speed of sound $\tilde{c}_\infty$, i.e. $M_\infty = \tilde{u}_\infty/\tilde{c}_\infty$. The system of equations is closed by an equation of state:

$$p = R\rho T. \tag{2.9}$$

For a calorically perfect gas, $R{=}\tilde{R}/\tilde{c}_p$ is the gas constant:

$$R = (\gamma - 1)/\gamma. \tag{2.10}$$

The free-stream speed of sound is defined as $\tilde{c}_\infty^2 = \gamma \tilde{R}\tilde{T}_\infty$. Using (2.9) and the non-dimensionalization for $\tilde{R}$, $\tilde{T}$ and $\tilde{\rho}$ as given above, it can be deduced that the non-dimensionalization of pressure $\tilde{p}$ is based on a reference pressure $\tilde{p}_{ref} = \tilde{\rho}_\infty \tilde{c}_\infty^2$. Here, the specific heat $c_p \equiv 1$. The gas properties k_e and μ depend on the temperature and are equal: $k_e = \mu$. The latter is computed from Sutherland's law, with a non-dimensional Sutherland's temperature $T_S = \tilde{T}_S/\tilde{T}_\infty$:

$$\mu = ((\gamma - 1)T)^{3/2}\frac{1 + T_S}{(\gamma - 1)T + T_S}. \tag{2.11}$$

For air (dimensional Sutherland's temperature $\tilde{T}_S = 110.4\,K$, see Anderson 2000), the T_S used here (see table 1) corresponds to a free-stream temperature of $\tilde{T}_\infty = 55.4\,K$. Finally, the internal enthalpy is proportional to the temperature $h = T$ and the internal energy $e = h - p/\rho$ is given by (again, note our temperature scale $(\gamma - 1)\tilde{T}_\infty$):

$$e = p/((\gamma - 1)\rho)\,. \tag{2.12}$$

To avoid confusion, we will not use indices to denote components in the three spatial dimensions below, for instance the velocity vector will only be referenced by $[u\ v\ w]^{\mathrm{T}}$ or by its components. Moreover, in all plots shown below the velocities are normalized by the free-stream velocity $\tilde{u}_\infty$ as this is a common practice in the literature. To represent the streamwise axis, a local Reynolds number $R_x = Re_x = \sqrt{xRe_\infty M_\infty}$ will be used.

2.2. *Numerical method*

The basis for the numerical method we use is an algorithm described by Nagarajan, Lele & Ferziger (2003), originally developed for transitional flow in subsonic conditions (Nagarajan, Lele & Ferziger 2007). Time-accurate solutions to the compressible Navier–Stokes equations, more precisely (2.1)–(2.12), are obtained using sixth-order compact finite differences in the interior of the domain with explicit third-order Runge–Kutta time stepping. The numerical discretization is constructed on a structured, curvilinear grid using staggered variables. The computational code is parallelized using MPI and has been run on a variety of computer architectures including shared-memory systems. For two-dimensional calculations, between 16 and 40 CPUs have been used while for three-dimensional simulations 32 CPUs were employed, resulting in a computational time of $\approx$0.364 s per time step with 40 CPUs ($NX = 1200$) in two-dimensional and $\approx$2.74 s in three-dimensional with 32 CPUs ($NX = 800$).

These simulations aim at capturing all relevant unsteady physical effects without further modelling and could therefore be denoted as direct numerical simulations. However, we will refer to them as 'numerical simulations' only, since any disturbances in the laminar flow remain small (linear) and no breakdown to turbulence occurs.

2.3. *Discretization, integration domains and boundary conditions*

We consider the flow over a flat plate (free-stream $u_\infty = u(y_2) = \tilde{u}_\infty/\tilde{c}_\infty = M_\infty$) with a localized two-dimensional roughness. The same set-up has been used in the numerical investigations of smooth walls (Eissler & Bestek 1996; Pagella *et al.* 2002). The origin of the coordinate system is located at the leading edge of the flat plate. The computational domain is placed downstream of the leading edge. The parameters for our test case are given in table 1.

At the inflow x_1, a self-similar boundary-layer solution is prescribed, while the wall boundary condition (BC) at y_1 is adiabatic for the base flow with a no-slip condition. Within a certain region close to the outflow x_2 and in the free-stream y_2, the solution is damped towards a laminar, self-similar state (sponge region). For three-dimensional simulations, periodicity in spanwise direction with a domain width $\lambda_z = 0.60415$ is assumed. Only a two-dimensional roughness is considered here. However, the interaction of such a roughness with a pair of oblique (three-dimensional) waves has been studied by means of three-dimensional simulations.

For the disturbances, both adiabatic and isothermal wall BCs have been considered and are compared below. In both these cases, the base flow is the same and has been computed with an adiabatic wall condition.

2.4. *Geometry and grid*

The shape of the roughness is defined by the following analytical function:

$$y_1(x) = \frac{h_R}{2} \sum_{k=-1}^{+1} k(\tanh(s_R(x - x_{0,k}))) \quad \text{with} \quad x_{0,k} = x_{c,R} - kl_R/2. \tag{2.13}$$

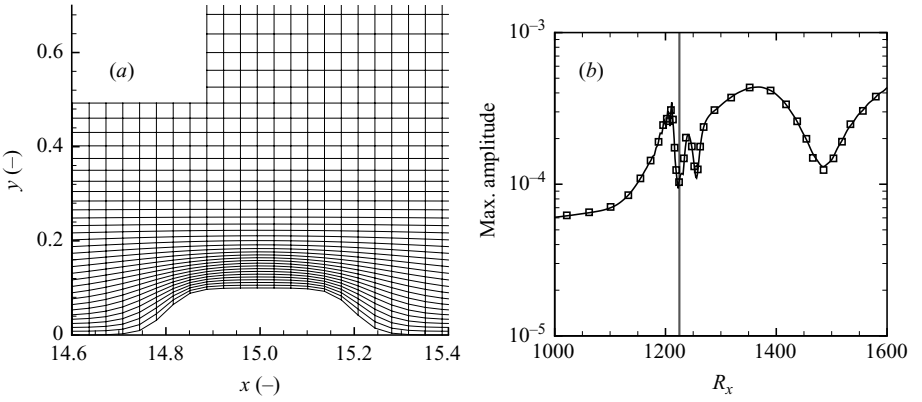

FIGURE 1. (*a*) Visualization of the grid in the vicinity of the roughness element. Only every second grid point in y is shown. (*b*) Streamwise evolution of maximum disturbance streamwise velocity for two different resolutions (and $x_2 = 30.1665$), $NX = 800$, $MY = 200$ (——), and $NX = 1600$, $MY = 400$ (□) (adiabatic boundary condition for the disturbance, $F = 1.0 \times 10^{-4}$). The roughness element of height $h_R = 0.1$ and length $l_R = 0.4$ is centred at $x_{c,R} = 15$ ($R_x = 1225$) as marked by a vertical line.

The values of s_R and $x_{c,R}$ are specified in table 1. The length l_R corresponds to the distance between the two inflection points in the roughness geometry. For the case depicted in figure 1(*a*), these inflection points are located at $x \approx 14.8$ and $x \approx 15.2$. A number of different roughness heights ($h_R = [0.01, 0.125]$) and lengths ($l_R = [0.4, 1.6]$) have been investigated.

The first (wall-parallel) grid line $m = 1$ collapses with the wall, i.e. it follows $y_1(x)$. In the streamwise and spanwise directions, it is subdivided with an equidistant spacing in the x and z directions with NX and KZ points, respectively. For all three-dimensional calculations we have chosen $KZ = 11$, otherwise $KZ = 0$. For these three-dimensional and a number of two-dimensional simulations, the streamwise domain length was reduced to $x_2 = 30.1665$ with $NX = 800$.

In the wall-normal direction, a grid stretching is applied, with the following formula holding at the inflow $n = 1$, with $\kappa = 0.25$ and $m = 1 \ldots MY$:

$$y(1, m) = y_1 \left((1 - \kappa) \left(\frac{m - 1}{MY - 1} \right)^3 + \kappa \frac{m - 1}{MY - 1} \right). \tag{2.14}$$

The coefficients appearing in this equation, together with the streamwise and wall-normal resolutions, are specified in table 1. The grid-stretching has been adjusted along the roughness; an example of the resulting grid is shown in figure 1(*a*).

2.5. *Disturbance forcing*

Disturbances of a fixed frequency are forced via blowing and suction at the wall upstream of the roughness element. The non-dimensional forcing frequency ω is defined as ($\tilde{f}$ is the dimensional frequency):

$$\omega = F M_\infty^2 Re_\infty, \quad \text{with} \quad F = 2\pi \tilde{f} \left(\tilde{\mu} / (\tilde{\rho} \tilde{u}^2) \right)_\infty. \tag{2.15}$$

The boundary condition at the wall is

$$(\rho v)_{wall} = A_v \sin(\omega t) \sin(16\,\xi) \exp\left(-\sqrt{2}/2\xi^2 \right), \quad \text{with} \quad \xi = (x - x_{c,strip})/L_{strip}. \tag{2.16}$$

$x_{c,strip}$	L_{strip}	ω	F	A_v	$Re_{x_{c,strip}}$
5.49	8.430	24	0.5×10^{-4}	2×10^{-4}	741
5.49	4.203	48	1.0×10^{-4}	2×10^{-4}	741
5.49	2.795	72	1.5×10^{-4}	2×10^{-4}	741

TABLE 2. Forcing parameters.

Forcing parameters, including $x_{c,strip}$ and L_{strip}, for different frequencies are given in table 2. The values of $x_{c,strip}$ and L_{strip} for the case $F = 1.0\times10^{-4}$ were chosen to match results of Pagella *et al.* (2002) for a flat plate, and then the strip length was doubled and halved for a forcing at twice and half this frequency (table 2). For a visualization of the disturbance in the region of the strip as resulting from (2.16), see Marxen, Iaccarino & Shaqfeh (2007). For simulations with three-dimensional disturbance input, the amplitude coefficient A_v in (2.16) is replaced by $A_v\cos(2\pi/\lambda_z z)$.

The time step for the numerical simulation was specified based on the frequency of the disturbance forcing ω. Here, we have chosen

$$\Delta t = \frac{2\pi}{\omega}\frac{1}{LP}, \tag{2.17}$$

with LP specified in table 1 for $\omega = 48$. The same Δt was used for the other forcing frequencies.

2.6. *Post-processing: Fourier analysis in time*

To analyse the instability of the boundary layer, results are Fourier transformed in time with a fundamental circular frequency $\Omega = \omega/2$. The corresponding discrete Fourier transform reads (here given only for the two-dimensional case, with $\mathrm{i} = \sqrt{-1}$):

$$\hat{s}_{hrm} = \frac{1}{50}\times\sum_{l=1}^{50} s(\mathbf{x}, t_l)\,\exp[2\,\mathrm{i}\,hrm\,\Omega\,t_l],$$
$$\text{with}\quad hrm = [0, 1/2, 1],\quad s = u, v, w, \rho, T, p, \tag{2.18}$$

where 50 samples are taken within two forcing periods, l is the sampling index and the discrete time is $t_l = 2/50\,LP\,l\Delta t$. The Fourier coefficient $\hat{s}_{hrm}(\boldsymbol{x})$ is complex, with an amplitude $|\hat{s}_{hrm}|$, and the phase is defined as

$$\Phi_{hrm} = \arctan(\mathrm{Im}(\hat{s}_{hrm})/\mathrm{Re}(\hat{s}_{hrm})). \tag{2.19}$$

The computations are advanced long enough so that the subharmonic $hrm = 1/2$ is at least an order of magnitude smaller than the first harmonic, thus demonstrating convergence towards a time-periodic state.

Only results for the first harmonic ($hrm = 1$) will be considered here. The streamwise disturbance amplification is quantified using wall-normal maxima of the amplitudes of a disturbance quantity $\hat{s}_1$, which are computed as

$$\hat{s}_1^{max}(x) = \max\{|\hat{s}_1(x = const, y)|\}. \tag{2.20}$$

The amplification rate α_i is computed from the streamwise velocity component

$$\alpha_i(x) = 1/\hat{u}_1^{max}\,\partial\hat{u}_1^{max}/\partial x. \tag{2.21}$$

The phase velocity is computed from the pressure ($s = p$ in (2.19), note that c_{ph} is non-dimensionalized by the free-stream velocity, i.e. $c_{ph} = \tilde{c}_{ph}/\tilde{u}_\infty = \tilde{c}_{ph}/(\tilde{c}_\infty M_\infty)$):

$$c_{ph} = Re_\infty M_\infty F\,(\partial\Phi_1/\partial x)^{-1}. \tag{2.22}$$

2.7. *Verification*

To assess the accuracy of the present code, we compared our computations with Pagella *et al.* (2002), who studied the growth of small disturbances in a flat-plate boundary layer at Mach 4.8 without a roughness element. The comparisons reported by Marxen *et al.* (2007) show very good agreement in all quantities of interest.

For the case with roughness, a grid study has been performed, showing the convergence of the present results for both the mean (not shown here, but see figure 1*a* of Marxen & Iaccarino 2008*b*) and disturbance quantities (figure 1*b*). Moreover, Marxen & Iaccarino (2008*b*) compared results for a body-fitted method using a non-orthogonal grid – as it is applied here – and an immersed boundary method based on a Cartesian orthogonal grid. They found good agreement between the two for both base flow and disturbance quantities.

The pressure rise across the shock, which develops downstream of the roughness, is not severe and, therefore, no shock-capturing scheme was required in the computations. Instead, the application of a high-order compact filter in streamwise and wall-normal directions is sufficient to stabilize the simulation without compromising the accuracy, as demonstrated by the grid study and also by a comparison of the steady-state base flow with a computation applying a Roe Riemann solver and a second order TVD scheme (Marxen & Iaccarino 2008*a*).

3. Base flow

To highlight the change in the steady-state laminar flow caused by a two-dimensional roughness element, a comparison between the flat-plate boundary layer with and without roughness is given. In particular, features that are absent for the smooth plate are pointed out in § 3.1. The influence of parameters such as the height and length of the roughness are briefly discussed in § 3.2.

3.1. *General features*

The case with a roughness having the height $h_R = 0.1$ and the (shortest) length $l_R = 0.4$ is regarded as the reference case and will be discussed in some detail. For this case, the ratio between the boundary-layer thickness δ_{99}, based on $\tilde{u}/\tilde{u}_\infty$=0.99 for the smooth flat plate at the centre location of the roughness ($x = 15$), and the height of the roughness is $h_R/\delta_{99} \approx 0.55$. Analogous relations for the boundary-layer displacement thickness δ^* and the momentum thickness θ are $h_R/\delta^* \approx 0.71$ and $h_R/\theta^* \approx 12.24$. A representation of the base flow field is given in figure 2 by means of numerical Schlieren images.

The roughness element causes a compression followed by an expansion, which again is followed by a compression. The latter causes a weak oblique shock downstream of the roughness element, well visible in figure 2(*a*). The expansion downstream of the roughness leads to an acceleration of the flow in the free stream (compare locations $x = 15$ and $x = 15.625$ for $y \in [0.22, 0.35]$ in figure 3). This acceleration causes the streamlines to turn towards the wall (figure 2*b*) after they have been deflected away from the wall by the roughness. Finally, downstream of the roughness the shock causes the streamlines to become roughly wall parallel again.

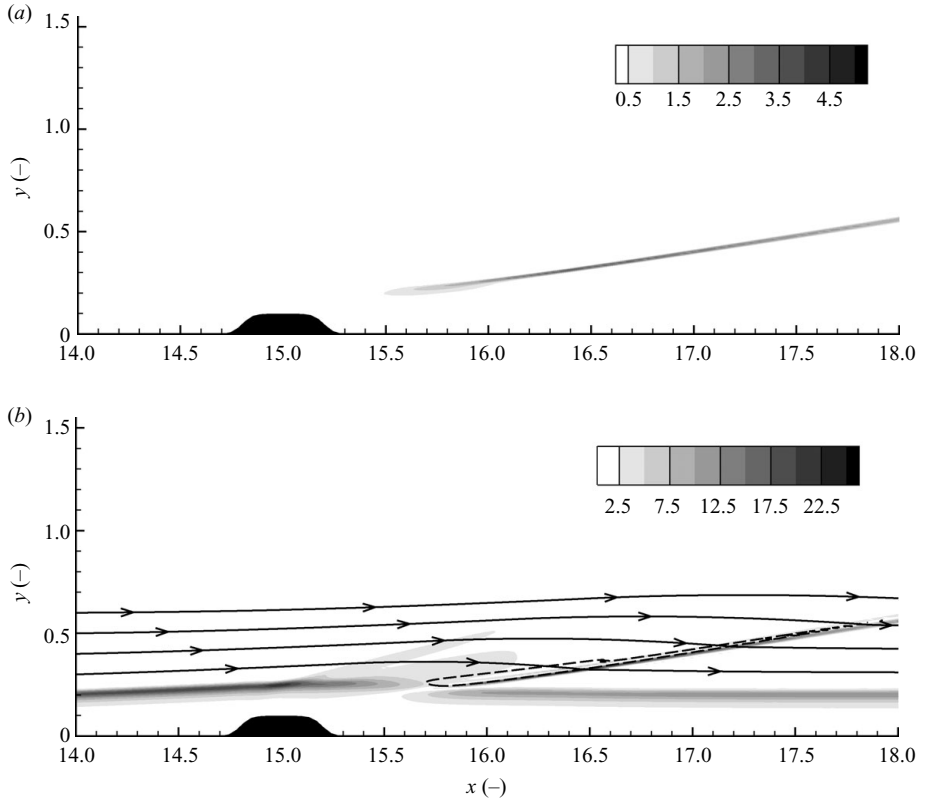

FIGURE 2. Computed Schlieren images for a roughness $h_R = 0.1$ and $l_R = 0.4$. (*a*) Contours of the positive streamwise density gradient $\partial p/\partial x > 0$. (*b*) Contours of the absolute wall-normal density gradient $|\partial p/\partial y|$, together with selected stream-lines outside of the boundary layer (→) and contour Mach 5.3 (– –).

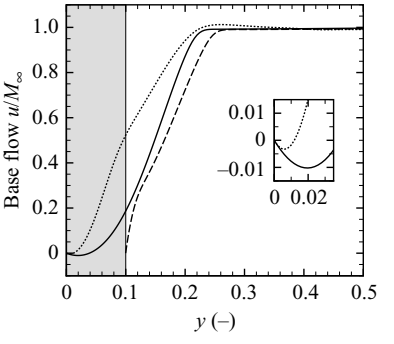

FIGURE 3. Base flow profiles of the *u*-velocity upstream of the smooth roughness at x=14.4 (R_x=1200) (——), at its centre $x = 15.0$ ($R_x = 1225$) (– –), and downstream of it at $x = 15.625$ ($R_x = 1250$) (· · · · · · ·), normalized with M_∞. The shaded area marks locations inside the body. The inset depicts the region close to the wall for x=14.4 and x=15.625 to highlight the reverse flow.

From figures 2(*a*) and 2(*b*) we can get a rough estimation of the shock angle σ. We will measure it with respect to a local streamline, noting that the streamlines are not exactly parallel to the wall. Based on the region between $x = 16.5$ and $x = 18$, the shock angle for our case is $\sigma \approx 12.3°$. In order to compare this value with the Mach angle, we have to take into account that the Mach number before the shock is slightly

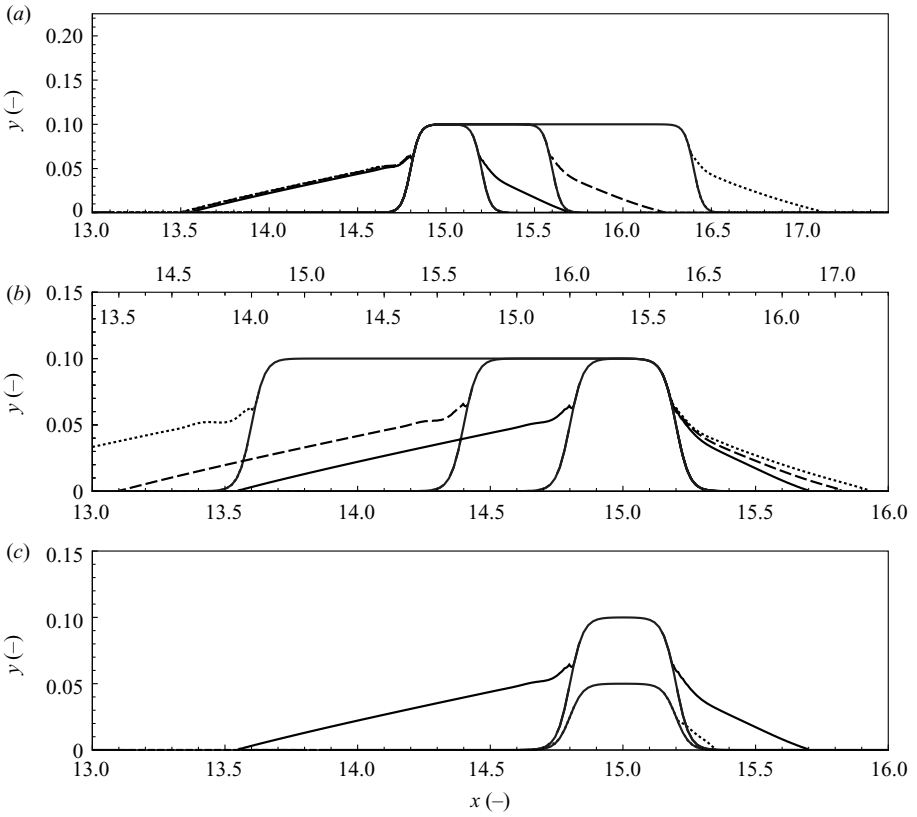

FIGURE 4. Contours of $u = 0$ for different roughness length with matching front ($h_R = 0.1$, figures 4*a* and 4*b*) as well as variation in the height of the roughness ($l_R = 0.4$, figure 4*c*). The wall-normal axis is enlarged by a factor of 5 compared with the streamwise axis. (*a*) Direct comparison, $l_R = 0.1$ (——), $l_R = 0.2$ (– –) and $l_R = 0.4$ (· · · · · · ·). (*b*) Same as figure 4(*a*), but with the streamwise axis adjusted to a matching back, respectively. (*c*) $h_R = 0.1$ (——) and $h_R = 0.05$ (· · · · · · ·).

higher than the free-stream Mach number due to the expansion. Here, its value is 5.3 (figure 2*b*), resulting in a Mach angle of $\arctan(5.3^{-1}) \approx 10.7^{\circ}$. This number deviates by only 10 % from the shock angle σ and hence suggests that we have a weak shock only.

The localized roughness element leads to boundary-layer separation in both the upstream and downstream regions. A small amount of reverse flow is visible in wall-normal profiles of the streamwise velocity (figure 3, inset). On top of the roughness, a thin attached boundary layer forms.

For $h_R = 0.1$, the length of the separation bubbles upstream and downstream differs roughly by a factor of two: its length is approximately $13h_R$ upstream of the roughness and $6h_R$ downstream of it (figure 4*c*). This observation is consistent with reports of Balakumar (2003) for a boundary layer at Mach 3.5.

3.2. *Variations of the roughness geometry*

To evaluate the sensitivity of the flow with respect to the geometry of the roughness, the effect of slight geometrical variations has been studied. In addition, this variation will be useful later to extract physical insights regarding disturbance evolution. More precisely, roughness length and position as well as height have been varied.

Results have been found to be relatively insensitive to the exact shape of the roughness (Marxen & Iaccarino 2008*b*). For instance, the length of the separation region in front of the roughness is only approximately 8 % longer for a sharp, rectangular-shaped roughness of the same height and volume as the present rounded roughness. Differences in amplification in front of the roughness are even less strong (see figure 14*b* of Marxen & Iaccarino 2008*b*).

3.2.1. *Length of the roughness*

Three different lengths, all with a height $h_R = 0.1$, have been simulated ($l_R = 0.4, 0.8, 1.6$). The centre location of the roughness has been varied in two ways for all these lengths. In the first way, the forward facing side is identical for all lengths, while in the second the backward facing side collapses. In the case of a matching front, the separation regions in front of the roughness are almost identical (figure 4*a*), while in the rear some small differences are visible (figure 4*b*). Calculations with a matching back revealed that the differences behind the roughness visible in figure 4(*b*) are due to the obstacle length and not its position with respect to the plate's leading edge. The independence of base-flow results with respect to slight variations in the position of the roughness is not surprising, since the growth of the boundary layer without roughness occurs on a much longer length scale compared with the length of the roughness, i.e. $R_x(x_{c,R}) \gg (R_x(x_{c,R} - l_R/2) - R_x(x_{c,R} + l_R/2))$.

3.2.2. *Height of the roughness*

Six different heights of the roughness with length $l_R = 0.4$ have been investigated ($h_R = 0.125, 0.1, 0.075, 0.05, 0.025, 0.0125$). In the case $h_R = 0.05$, we observe that both the separation regions in the front and the back have been reduced considerably relative to the $h_R = 0.1$ case (figure 4*c*). It is consistent with Balakumar (2003) that for $h_R = 0.05$ the separation region behind the roughness is larger than the one in front (the latter is so small that it is not even visible in figure 4*c*) – while for the higher roughness $h_R = 0.1$ the opposite was true. The length of the separation zone in the back for $h_R = 0.05$ is smaller than the one for $h_R = 0.1$ by a factor of ~ 3.3, again similar to the value ~ 3.4 reported by Balakumar (2003).

4. Boundary-layer instability and disturbance evolution

In the last section, we have seen that the roughness modifies the base flow through non-local (pressure) effects, causing recirculation upstream and downstream. In light of results from Pagella *et al.* (2002, 2004) the instability of the boundary layer (when compared with the smooth plate) is expected to be profoundly changed as well. We note that we did not observe an absolute or global instability as in Robinet (2007). Such an occurrence would have prevented the undisturbed laminar flow from attaining a converged steady state.

The steady-state laminar flow fields for different roughness heights will be used as a base flow for subsequent investigations of convective instability of a small-amplitude perturbation. We apply two different methods. First, a local linear stability analysis shall help us to get an overall impression on how a two-dimensional roughness alters the instability of the boundary layer. Second, results from numerical simulations are presented, in which a small-amplitude perturbation is forced by means of blowing and suction at the wall.

Main emphasis is put on results from numerical simulations, while the downstream evolution of the resulting boundary-layer disturbance will also be compared between

the two approaches. This comparison can aid in the interpretation of the flow dynamics. While it is understood that a theoretical approach based on the parabolized stability equations (Herbert 1997) may result in a closer matching of numerical and theoretical results, we regard the theoretical approach employed here as sufficient to gain a better understanding of the flow dynamics.

A linear stability analysis is presented first (§ 4.1), followed by a discussion of results from a variety of numerical simulations with disturbance forcing. The discussion is grouped according to three different regions with respect to the roughness. First, the disturbance evolution in front of the roughness is discussed (§ 4.2) in order to investigate the effect of flow separation on the amplification and to assess the accuracy of LST for describing disturbance evolution in separating boundary layers. Next, the flow field downstream of the roughness is considered (§ 4.3). A comparison of numerical results and LST can help to identify mechanisms of disturbance growth in the downstream region. Finally, the evolution in the vicinity of the roughness is inspected (§ 4.4). In this region, LST is not applicable due to rapid changes in both base flow and disturbance, and therefore our investigation relies entirely on the full Navier–Stokes equations.

The disturbance amplitude in all cases considered here is sufficiently small as to not cause a significant mean flow deformation. This deformation was checked to be of the order of 10^{-6} for a perturbation amplitude of the order of 10^{-3}. A differentiation between the stability of the base flow and that of the mean flow, that is, the time average of the disturbed flow, as done for example by Sipp & Lebedev (2007), is therefore not necessary.

Finally, we have to point out that only one specific set of parameters has been considered here, in particular regarding the choice of Mach number and the location of roughness (i.e. $Re_{x_{c,R}}$).

4.1. *Linear stability analysis*

LST analyses are carried out using a shooting method developed and implemented by Mack (1969). This method solves the spatial linear stability problem: for a fixed (real) frequency, it computes a single complex eigenvalue. This eigenvalue is composed of a streamwise wavenumber (real part) $\alpha_r = \omega/(c_{ph}M_\infty)$ (note that c_{ph} has been non-dimensionalized by the free-stream velocity, i.e. $c_{ph} = \tilde{c}_{ph}/\tilde{u}_\infty = \tilde{c}_{ph}/(\tilde{c}_\infty M_\infty)$, see (2.22), while ω has been normalized using the free-stream speed of sound; see (2.15)) and streamwise amplification rate (imaginary part) α_i. Emphasis is placed on examining two-dimensional disturbances, as these are the most amplified ones for the present set-up. A brief discussion of oblique (three-dimensional) waves is also given. In the stability calculations, an isothermal boundary condition has been used. They are based on the steady-state flow fields as discussed in § 3.

4.1.1. *Stability diagrams for a two-dimensional disturbance*

Amplification rates α_i for selected roughnesses are given in figure 5. For reference, the stability of the flat plate without roughness is also depicted (figure 5*a*). The roughness causes the region of second-type instability (the upper dark region in the stability diagrams) to shift towards lower frequencies. The overall maximum amplification rate is larger with roughness as compared with the flat-plate case, and this maximum is located within the separation region upstream of the roughness.

The roughness with a lower height has a weaker effect on the instability, not only in terms of the affected R_x range but also with regard to the maximum amplification rate (compare figures 5*b* and 5*c*). As expected from the base flow

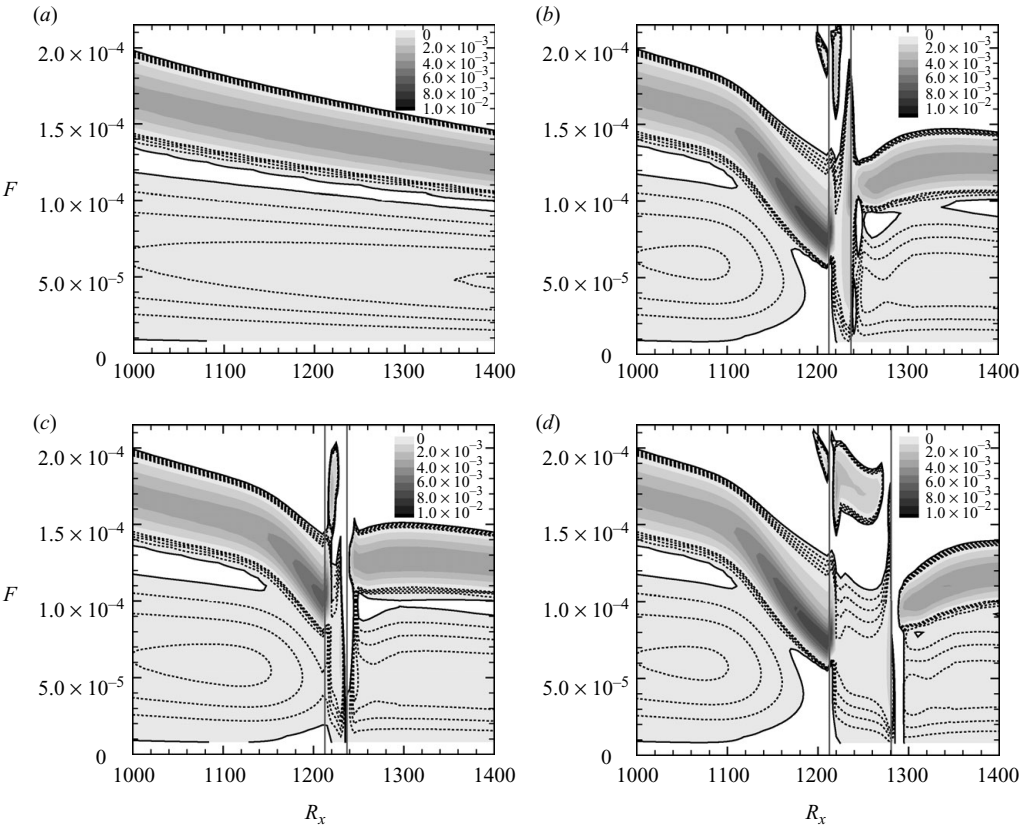

FIGURE 5. Stability diagrams for two-dimensional perturbations (amplification rate $\alpha_i \times R_x/Re_\infty$ from LST). Line contours range from 0 to 0.0005 with $\Delta = 0.000125$. The vertical lines mark the locations x where $y_1 = h_R/2$ and in their vicinity the LST results may be invalid. (*a*) Flat plate. (*b*) Roughness with $h_R = 0.1$ and $l_R = 0.4$. (*c*) Roughness with $h_R = 0.05$ and $l_R = 0.4$ and (*d*) roughness with $h_R = 0.1$ and $l_R = 0.6$.

(§ 3.2), the instability in front of the roughness is independent of the (downstream) length of the roughness (compare figures 5*b* and 5*d*), while some differences are visible in the region downstream of the roughness.

4.1.2. *Oblique (three-dimensional) waves*

Stability diagrams for oblique (three-dimensional) spanwise waves are depicted in figure 6. The most amplified first-type instability wave possesses a non-zero spanwise wavenumber (figure 6*a*). Nevertheless, inside the separation bubble in front of the roughness, the second-type instability is still stronger than the first-type instability. This is true even at the spanwise wavenumber where the first-type instability exhibits maximum amplification ($\beta \approx 0.08$ in figure 6*b*).

In contrast to the frequency range, the range of amplified spanwise wavenumbers increases due to the roughness (compare figures 6*b* and 6*c*). The overall maximum amplification for first-type instability modes is shifted towards larger spanwise wavenumbers (figure 6*a*). It was also found that the streamwise wavenumber increases, so that the (shifting) effect on the obliqueness angle is less pronounced.

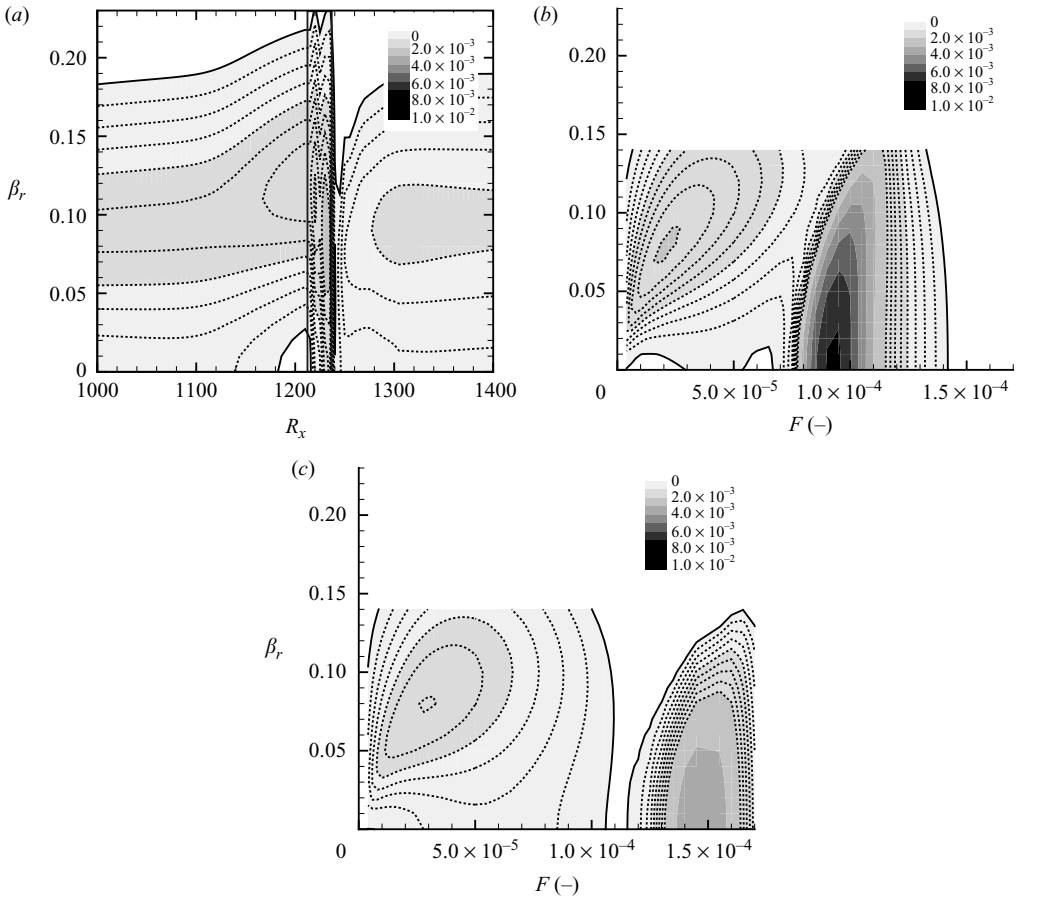

FIGURE 6. Stability diagrams for varying spanwise wavenumbers $\beta_r = 2\pi/\lambda_z \times R_x/(Re_\infty M_\infty)$. While the greyscales are the same as in figure 5, the contour lines span an interval 0 to 0.005 with $\Delta = 0.00025$. (*a*) $F = 0.5 \times 10^{-4}$, roughness with $h_R = 0.1$ and $l_R = 0.4$. (*b*) $R_x = 1180$, roughness $h_R = 0.1$, $l_R = 0.4$. (*c*) $R_x = 1180$, flat plate.

LST results suggest that, with roughness, the first-type instability is reduced for two-dimensional waves when compared with the flat plate. For instance, at $R_x = 1200$, these waves are even predicted to be damped (see the white region in the lower part of figure 6*a*). Pagella *et al.* (2002) made a similar observation for their case of shock–boundary-layer interaction, but also acknowledged that a first-mode instability should be present since a generalized inflection point exists. Despite this observation of an inflection point, in a follow-up paper, Pagella *et al.* (2004) argued that the first-type instability mode is stabilized. However, if we include oblique (three-dimensional) waves in the analysis, we see that LST predicts an increase in the first-type amplification for non-zero spanwise wavenumbers, i.e. a destabilization of the most important oblique first-type instability waves by the two-dimensional roughness.

4.2. *Disturbance evolution in the separating boundary layer in front of the roughness*

The evolution of disturbances shall now be analysed by means of integrating the Navier–Stokes equations in time. Disturbances have been forced via blowing and suction upstream of the roughness as described in § 2.5, and their evolution is studied using a Fourier analysis (see § 2.6).

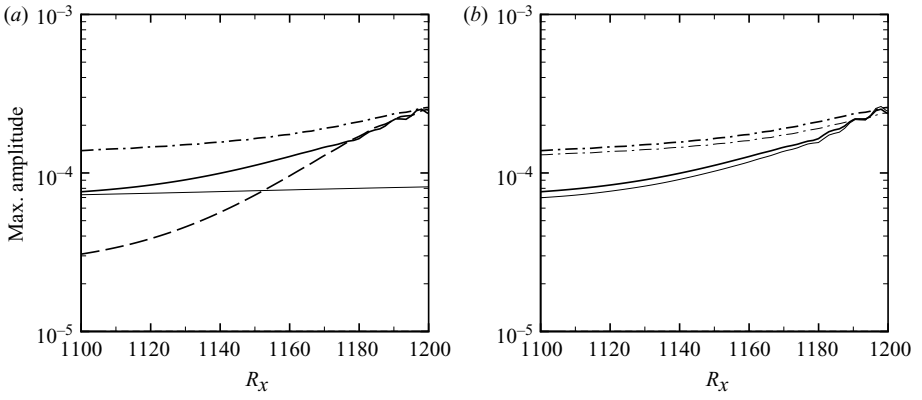

FIGURE 7. Streamwise evolution of the maximum amplitude in the Navier–Stokes simulation for $F = 1.0 \times 10^{-4}$: temperature $0.1 \times \hat{T}_1^{max}$ (–·–·–), streamwise velocity $\hat{u}_1^{max}$ (——) and wall-normal velocity $\hat{v}_1^{max}$ (– –). (*a*) Roughness $h_R = 0.1$, $l_R = 0.4$ (thick lines) vs. flat plate (thin line) for an isothermal BC. (*b*) Isothermal (thick lines) vs. adiabatic (thin lines) BC for a roughness $h_R = 0.1$, $l_R = 0.4$.

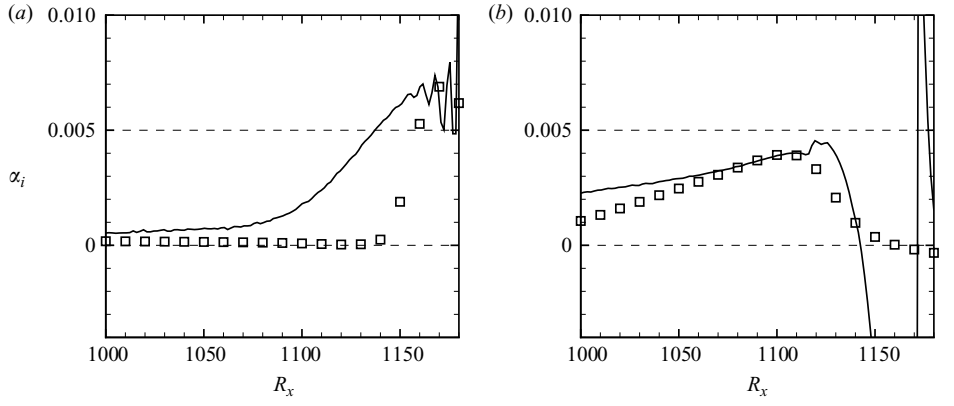

FIGURE 8. Comparison of amplification rates $-\alpha_i$ between Navier–Stokes simulation with isothermal BC (——) and LST (□), roughness with $h_R = 0.1$ and $l_R = 0.4$. $F = 1.0 \times 10^{-4}$ (*a*) and 1.5×10^{-4} (b).

4.2.1. *Simulation results and comparison with LST*

The amplification for $F = 1.0 \times 10^{-4}$ increases strongly upstream of the roughness element as compared with the case without roughness (figure 7*a*). Differences between an adiabatic and an isothermal condition for the disturbance are small (figure 7*b*). Regarding amplification rates (figure 8) in the zone where we see a difference between the flat plate and the roughness case ($R_x > 1050$), quantitative agreement between LST and Navier–Stokes simulation results derived from $\hat{u}_1^{max}$ is good whenever the disturbance possesses second-type instability characteristics. This is the case for $F = 1.0 \times 10^{-4}$ closer to the roughness ($R_x \gtrapprox 1160$), while for $F = 1.5 \times 10^{-4}$ this is true farther upstream of the roughness ($R_x \lessapprox 1160$).

Upstream of $R_x \lessapprox 1160$, the disturbance at $F = 1.0 \times 10^{-4}$ exhibits first-type instability characteristics, which was inferred from the fact that no change in phase for the pressure amplitude function occurs along y. In this region of first-type

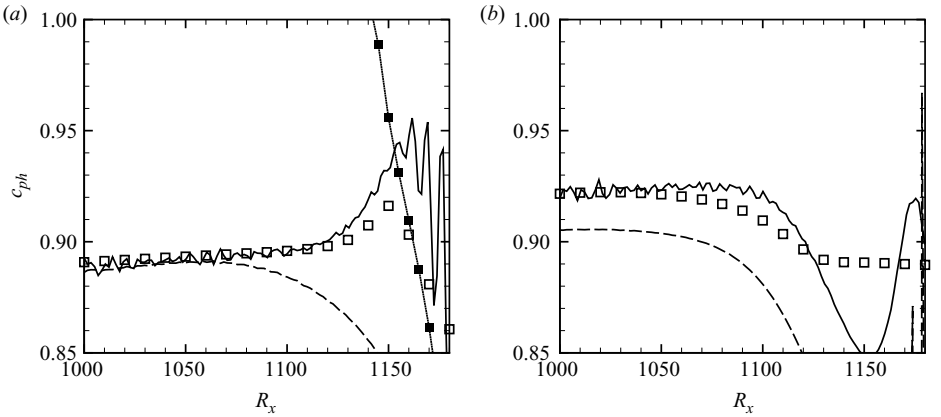

FIGURE 9. Comparison of phase velocities c_{ph}, based on the pressure, between Navier–Stokes simulation with isothermal BC (– –$y = 0$, ——$y = 0.13$) and LST amplified mode (□) and LST stable mode 1–2 (· · · · · ·■ · · · · · ·), roughness with $h_R = 0.1$ and $l_R = 0.4$. $F = 1.0 \times 10^{-4}$ (*a*) and 1.5×10^{-4} (*b*).

characteristics, the amplification of the two-dimensional wave is considerably under predicted by LST (figure 8*a*).

Regarding the two-dimensional first-type instability, the underprediction of amplification can likely be explained by non-parallel effects. Pagella *et al.* (2002) provided evidence that this is true for a flat-plate boundary layer, and we believe that it is even more pronounced here as a result of separation.

Phase velocities in the region of first-type characteristics obtained away from the wall compare well with LST upstream of the roughness (solid lines in figure 9*a* for $R_x \lessapprox 1160$ at $F = 1.0 \times 10^{-4}$). However, phase velocities for $F = 1.0 \times 10^{-4}$ in the region of second-type characteristics in front of, but close to, the roughness for $R_x \gtrapprox 1160$ are underpredicted by LST (figure 9*a*). Additional evidence for the latter conjecture can be found in figure 9(*b*), if we keep in mind that the disturbance at the higher frequency $F = 1.5 \times 10^{-4}$ is located in the region of the second-type instability for all R_x (again, solid lines). A systematic deviation of phase velocities between the Navier–Stokes simulation and LST occurs near the wall in the second-type regions (see dashed lines in figure 9).

Similar to the phase velocities, the agreement of amplitude functions for the first-type instability is very good upstream of the roughness (figures 10*a* and 10*b*). It is slightly better than for a perturbation with second-type characteristics at the same streamwise location (figures 10*c* and 10*d*). The differences for the mode with second-type characteristics visible in figure 10(*c*) for $\hat{u}_1$ and in figure 10(*d*) for $\hat{T}_1$ are consistent with those of Pagella *et al.* (2002). In particular, LST overpredicts the $\hat{T}_1$-maximum (figure 10*d*) and the level of $\hat{u}_1$ in the free stream (figure 10*c*). Note that in figure 10 (and again in figure 16), all amplitude functions have been normalized by a constant factor. Such a procedure is allowed and reasonable due to the linearity of the disturbance. The factor has been chosen to be the maximum (non-dimensional) streamwise velocity disturbance $\max|\hat{u}_1|$ at the respective x-location (denoted by u_{max} in the axis title).

Qualitatively, the same differences can be observed for $F = 1.0 \times 10^{-4}$ once the corresponding disturbance lies in the region of second-type instability farther downstream (figures 10*e* and 10*f*), albeit these differences are much more pronounced.

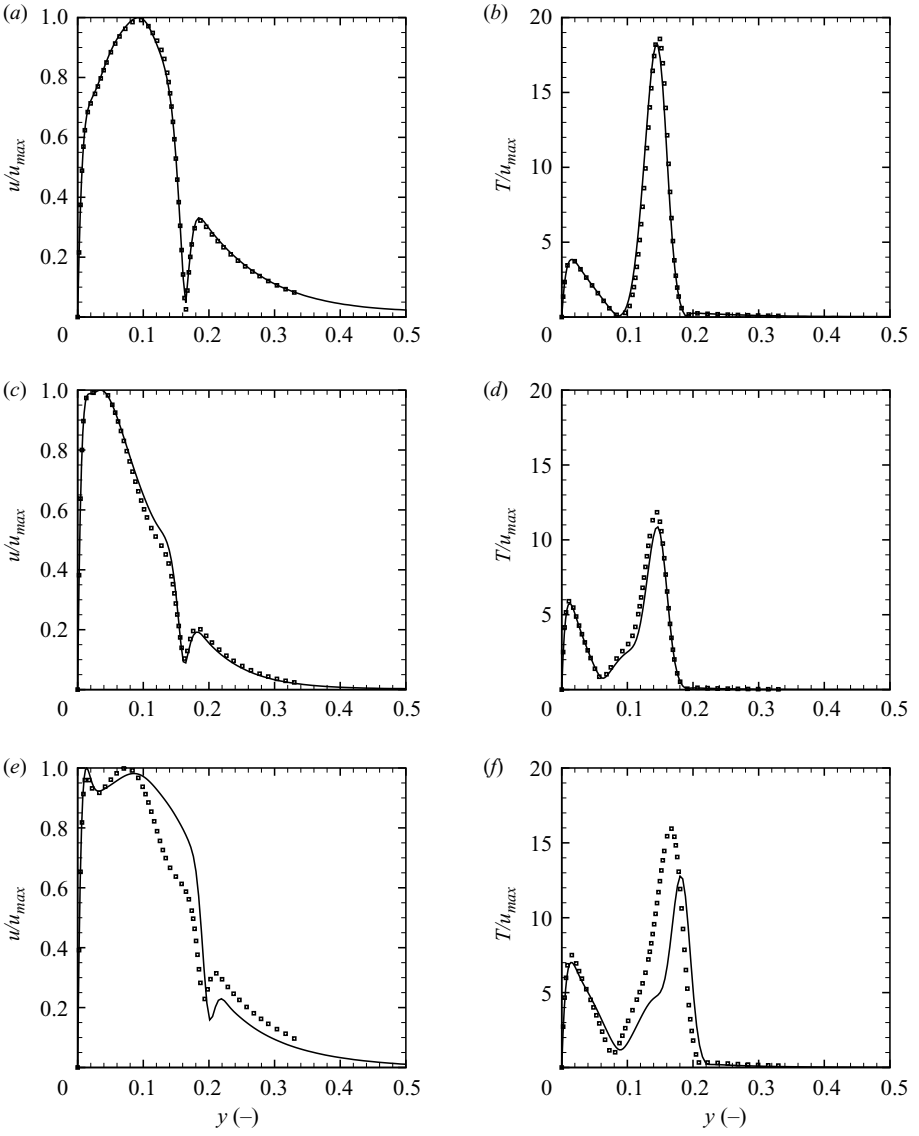

FIGURE 10. Wall-normal functions, roughness with $h_R = 0.1$ and $l_R = 0.4$. LST (○) and Navier–Stokes simulation with isothermal BC (——). (*a*) $|\hat{u}_1|$ at $R_x = 1100$, $F = 1.0 \times 10^{-4}$. (*b*) $|\hat{T}_1|$ at $R_x = 1100$, $F = 1.0 \times 10^{-4}$. (*c*) $|\hat{u}_1|$ at $R_x = 1100$, $F = 1.5 \times 10^{-4}$. (*d*) $|\hat{T}_1|$ at $R_x = 1100$, $F = 1.5 \times 10^{-4}$. (*e*) $|\hat{u}_1|$ at $R_x = 1180$, $F = 1.0 \times 10^{-4}$. (*f*) $|\hat{T}_1|$ at $R_x = 1180$, $F = 1.0 \times 10^{-4}$.

Hence, these differences in amplitude functions are reasonably explained as a result of non-parallel effects and are more pronounced for modes with second-type characteristics.

Further confirmation for LST's underprediction of amplification rates in the first-type region comes from a simulation with $F = 0.5 \times 10^{-4}$, for which the disturbance lies in the first-type region within the entire domain in front of the roughness (figure 11*a*). For this frequency, LST predicts even qualitatively wrong trends regarding amplification rates: while the disturbance is more strongly amplified due

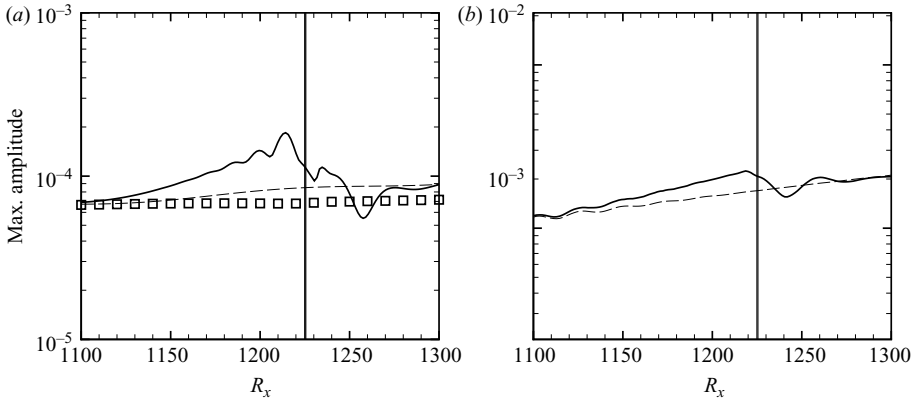

FIGURE 11. Streamwise evolution of $\hat{u}_1^{max}$ with forcing at $F = 0.5 \times 10^{-4}$. Roughness with $h_R = 0.1$, $l_R = 0.4$ (——), flat plate (– –) and integrated amplification rates from LST for the base flow *with* roughness $h_R = 0.1$, $l_R = 0.4$ (□). (*a*) Two-dimensional wave, isothermal BC for the disturbance. (*b*) Oblique (three-dimensional) wave, adiabatic BC, with $2\pi/\lambda_z = 10.4$ (at $R_x = 1180$, this corresponds to $\beta_r = 0.1227$).

to the separation, LST predicts less amplification than that for the flat plate as highlighted in § 4.1.2. A possible reason for this deficiency of LST is associated with the streamwise wavelength of the disturbance, which increases with decreasing frequency and, therefore, the parallel-flow assumption in the theory becomes more strongly violated, especially in the vicinity of the roughness. Interestingly, while the increase in amplification is qualitatively the same for two-dimensional and oblique (three-dimensional) waves (compare figures 11*a* and 11*b*), this increase is quantitatively more pronounced for the two-dimensional wave. For that reason, we will not further consider oblique (three-dimensional) waves. In the oblique-wave case also LST predicts a destabilization (compare figures 6*b* and 6*c*).

To understand the LST results regarding the different qualitative predictions for two-dimensional and three-dimensional waves, the alteration of the amplification rate may be regarded as caused by the sum of (separate) contributions from opposite effects induced by the separating boundary layer. A stronger inflectional instability may be overcompensated in the LST by a reduction in the amplification rate associated with a stronger non-parallel effect. This effect is more pronounced for two-dimensional waves and causes the resulting amplification rate to lie below the flat-plate value.

In summary, the overall good agreement of phase velocities and amplitude functions between LST and numerical simulation even in the separation region in front of the roughness suggests that LST is a useful tool for the interpretation of numerical results. However, a less good agreement is seen with respect to amplification rates, in particular LST fails to fully capture the destabilization of a first-type instability in the separation region.

Lastly, based on the evidence presented here, we cannot exclude that the increased amplification as seen in the numerical results is associated with the non-normality of the modes, i.e. transient growth. Such an effect will be discussed for the region behind the roughness in § 4.3.2. One way to clarify this issue may be to apply a multi-mode decomposition (Tumin *et al.* 2007), together with a theoretical approach capable of handling non-parallel base flows.

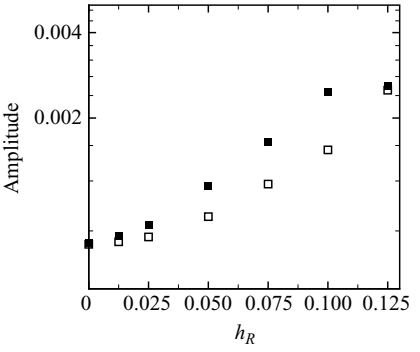

FIGURE 12. Maximum amplitude (streamwise velocity) with forcing at $F = 1.0 \times 10^{-4}$ as a function of the height of the roughness h_R at $R_x = 1180$ (□) and $R_x = 1200$ (■) from Navier–Stokes simulations with adiabatic BC, $l_R = 0.4$ for all cases.

4.2.2. *Physical mechanisms of disturbance growth*

The alteration of instability caused by the separation region in front of the roughness can be explained by the changed base-flow profiles. The effect of changes in the base flow has been studied before, and we will apply the respective findings to our case in order to explain the observed alteration.

Referring to a second-type instability, Malik & Anderson (1991) describe that: 'Anything that thins the boundary layer decreases the wavelength and thus increases the frequency and the converse is also true'. Indeed, we observed that the region of second-type instability moves to lower frequencies, which is therefore due to the boundary-layer thickening caused by separation.

According to Pagella *et al.* (2002), an increased disturbance amplification is caused by the displacement of the shear layer away from the wall, diminishing the stabilizing influence of viscosity. This conjecture is in agreement with an earlier analysis by Mack (1975) regarding the influence of alterations in boundary-layer thickness by, for example, constant suction at the wall or pressure gradients. This argument applies to both first- and second-type instabilities, as the instability mechanism in both cases is essentially of an inviscid nature for the present Mach number.

Referring specifically to the region of second-type instability characteristics, Pagella *et al.* (2002) pointed out that '... another portion of the total rise of ... instability can be assumed to be caused by the increase of thickness in this local supersonic regions.' (p. 2093) This latter effect is absent for a first-type instability mechanism. This absence therefore offers an explanation as to why we see a stronger increase (when compared with the flat plate, respectively) in amplification for the second-type instability (figure 7) than that for the first-type instability (figure 11). In summary, we believe that two main mechanisms are at work altering the instability: a diminishing influence of viscosity (first and second type) and the increase in thickness of the local supersonic regions (affecting only the second type).

4.2.3. *Influence of the roughness height*

The effect of the height h_R on the disturbance evolution in front of the roughness has been studied only for adiabatic wall boundary conditions for the disturbance. This effect turns out to be as expected in light of the explanations in the previous section: A higher roughness translates to stronger separation accompanied by stronger amplification in front of the roughness (figure 12). For a fixed frequency, there exists

a height of the roughness leading to the largest amplitude just upstream of the roughness. Further increasing the roughness height does not further increase the gain in amplitude as the (second-type) instability region is pushed towards lower frequencies and the amplification rate is reduced or even becomes negative (indicating damping) in front of the roughness.

These results suggest that for a fixed frequency, a most dangerous height exists if we consider streamwise integrated amplification. However, this statement may only be valid as long as the roughness is not too high, and no attempts were made here to increase the height beyond the boundary-layer edge.

4.3. *Disturbance evolution downstream of the roughness*

In the introduction (§ 1) it was pointed out that the roughness may indirectly act as an oscillator becoming a source of boundary-layer perturbations that are absent otherwise. If they exist, these perturbations may be observable downstream of the roughness. This section demonstrates that additional perturbations can be generated even in the absence of a global instability of the type considered by Robinet (2007). These additional perturbations may be important even if they are stable due to transient-growth effects. Upon interaction with those coming from upstream, they can cause the total disturbance amplitude behind the roughness to increase significantly. This could induce early onset of nonlinear effects.

One possible interaction is a constructive interference of normal modes similar to the beat discussed in the introduction, an effect that will be temporary and may therefore indeed be classified as transient growth (see § 4.3.2). The second possible, but entirely different, interaction is a conversion of an additional stable disturbance into the (original) amplified disturbance. In this situation, the amplitude of the original wave will increase permanently so that this effect is important even far downstream (see § 4.3.5). Both mechanisms can occur simultaneously and are explored in the following. Third, a complex interaction of the disturbance with a rapidly changing boundary layer in the vicinity of the roughness may occur and cause a sudden amplification boost (see § 4.4.3).

4.3.1. *Numerical results and comparison with LST*

The linear stability results of § 4.1.1 showed that stability properties upstream and downstream of the roughness are similar. The most important observation was an increased amplification for the second-type instability mechanism, which is also shifted to lower frequencies (see e.g. figure 5*b*). Therefore, we might expect that the region of displaced boundary layer downstream of the roughness causes a similar disturbance evolution as the zone upstream of it (see § 4.2.1) – where overall good agreement between the Navier–Stokes simulation and LST was found for the second-type instability. Yet, downstream of the roughness, we see an alternating strong increase and decrease in disturbance amplitudes instead (figure 13). It does not at all resemble the behaviour of the most amplified mode from LST – even if we account for the systematic differences between LST and Navier–Stokes simulation to be expected in light of § 4.2.1. The oscillating pattern is particularly visible for near-wall maxima as they occur for $\hat{u}_1$ or $\hat{v}_1$ but not for $\hat{\rho}_1$ or $\hat{T}_1$ (figure 13*a*). It is more pronounced for the adiabatic BC as compared with the isothermal BC (figure 13*b*).

Pagella *et al.* (2002) made a similar observation downstream of the separation zone caused by shock–boundary-layer interaction. They also noted a change in the speed of wave propagation. The evolution of wall-pressure perturbations in our case (dashed lines in figure 14) is in complete qualitative agreement with their

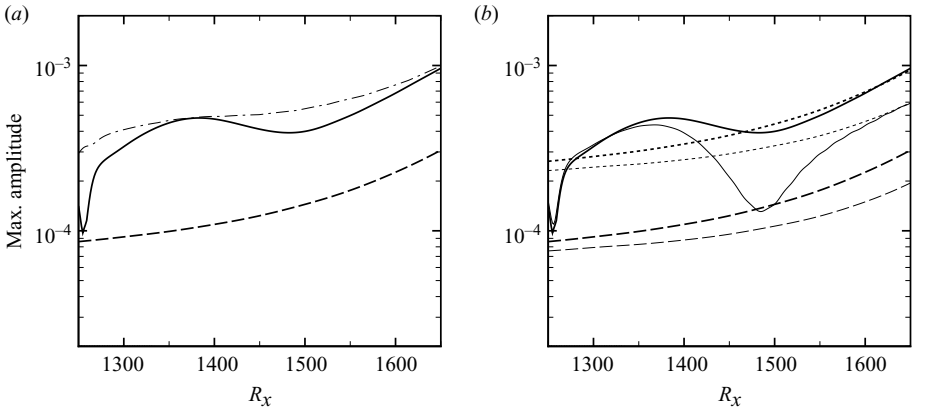

FIGURE 13. Streamwise evolution of the maximum amplitude in the Navier–Stokes simulation with forcing at $F = 1.0 \times 10^{-4}$: temperature $0.1 \times \hat{T}_1^{max}$ (–·–·–), streamwise velocity $\hat{u}_1^{max}$ with (——) and without (– –) roughness. The roughness with $h_R = 0.1$ and $l_R = 0.4$ is located slightly upstream of the depicted streamwise range of R_x. (*a*) Isothermal BC. (*b*) Isothermal (thick lines) vs. adiabatic (thin lines) BC. Dotted lines (· · · · · · ·) correspond to $\hat{u}_1^{max}$ for a flat plate, but are shifted by a factor of 3.06.

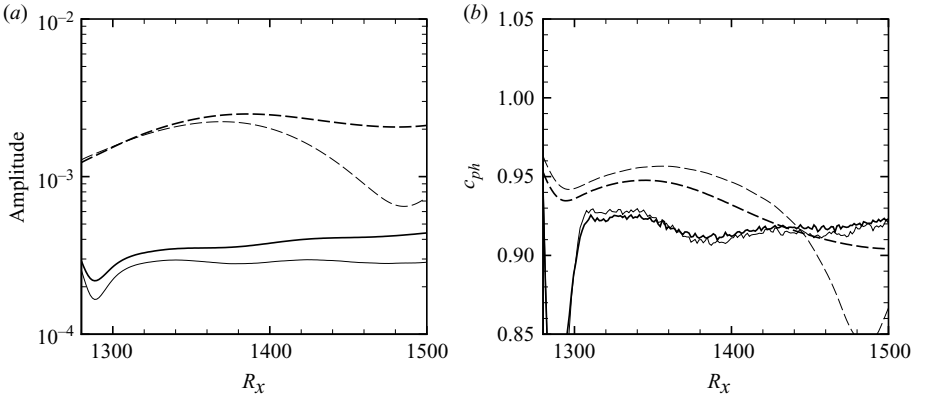

FIGURE 14. Comparison between Navier–Stokes simulation with different wall boundary conditions for $F = 1.0 \times 10^{-4}$, roughness with $h_R = 0.1$ and $l_R = 0.4$. Navier–Stokes solution at $y = 0.0$ (– –) and $y = 0.2$ (——). Thick lines denote isothermal boundary condition for the disturbance, and thin lines denote adiabatic boundary condition for the disturbance. (*a*) Streamwise evolution of $|\hat{p}|$. (*b*) Phase velocities c_{ph}.

observations. In the region away from the wall (solid lines in figures 14 and 15) however, favourable agreement of the pressure perturbation with the amplified mode from LST (open symbols) is found for both streamwise-integrated amplification rate and phase velocities—already shortly downstream of the roughness for $R_x > 1300$ with a slight underprediction of c_{ph} from LST in the interval $R_x \in [1310, 1360]$ (figure 15).

Results for an isothermal boundary condition for the disturbance exhibit a larger amplification for both flat plate and with a roughness. The larger amplitude observed far downstream in the case of an isothermal BC as compared with the adiabatic BC can be explained by this difference in amplification (see the dotted lines in figure 13*b*).

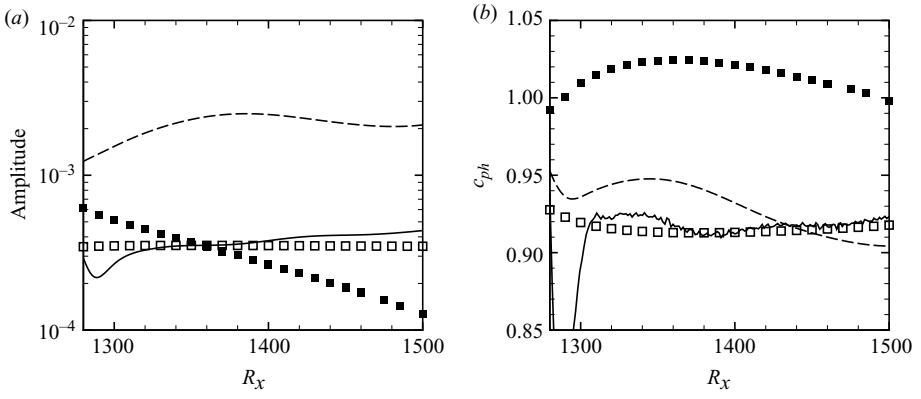

FIGURE 15. Comparison between Navier–Stokes simulation with isothermal BC for $F = 1.0 \times 10^{-4}$ and LST, roughness with $h_R = 0.1$ and $l_R = 0.4$. LST amplified mode (□), LST mode 1–2 (■), Navier–Stokes solution at $y = 0.0$ (– –) and $y = 0.2$ (——). (*a*) Streamwise evolution of $|\hat{p}|$. (*b*) Phase velocities c_{ph}.

4.3.2. *Physical mechanisms of disturbance growth*

The good agreement between the Navier–Stokes simulation and LST away from the wall (figure 15) indicates that the total perturbation signal indeed contains the amplified mode. However, disagreement at the wall suggests that this mode cannot be the only contribution. Instead, the signal may be composed of (an) additional mode(s) of the same frequency resulting in a beat. Eissler & Bestek (1996) demonstrated that blowing and suction at the wall can excite what we call the stable mode 1–2, and the interaction of the stable and the unstable modes was, as they could show, responsible for a beat they observed. Since the wall signature that they observed resembles that witnessed in our calculations for flow behind the roughness element, we were motivated to check whether the same physical mechanism is at work in our application.

In order to render such an explanation plausible, the stable mode 1–2 has to meet certain requirements. First, it has to have a similar amplitude function close to the wall as the amplified mode, but decay to zero much more quickly away from the wall. Figure 16 demonstrates that this is true for the present case indeed (see for instance also figure 7 of Fezer & Kloker 2002). A superposition could explain why at one location the amplitude function near the wall from numerical simulation is larger than the instability mode from LST (figure 16*a*). Slightly downstream at $R_x = 1500$, LST and numerical results for the isothermal BC match, while numerical pressure amplitude functions for the adiabatic BC are even significantly smaller (figure 16*b*). This latter observation can explain why a more pronounced beat is observable in the adiabatic case.

Second, the amplification rates of both the unstable and the stable modes should be sufficiently small for a significantly long distance so that both waves keep a comparable amplitude for a non-negligible downstream distance. Even though the stable mode 1–2 is predicted by LST to be damped at a non-negligible rate (figure 15*a*, filled symbols), results in Ma & Zhong (2003*a*) for a mode 2–3, which is similar in character to mode 1–2, suggest that a numerical simulation may exhibit a much weaker decay rate than the one predicted by LST (as much as 50 %; see figure 26 of Ma & Zhong 2003*a*). For that reason, the actual disturbance may not be as strongly damped as suggested by LST and may persist much farther downstream. Results of

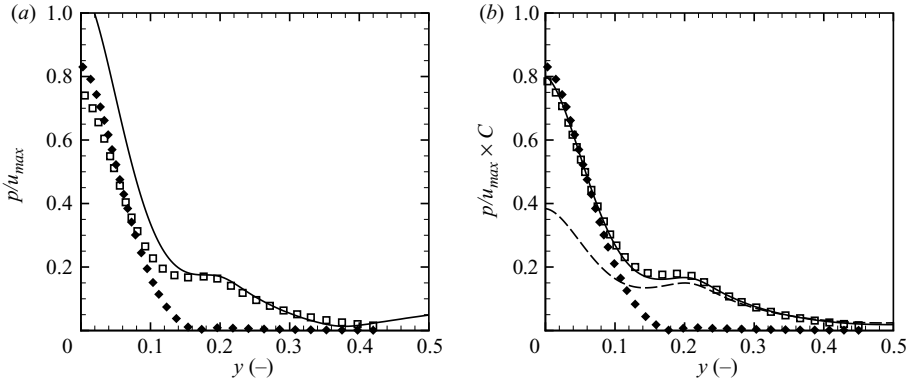

FIGURE 16. Wall-normal functions $|\hat{p}_1|$ for the forcing frequency $F = 1.0 \times 10^{-4}$, roughness with $h_R = 0.1$ and $l_R = 0.4$. LST amplified mode (□), LST mode 1–2 (◆), lines: Navier–Stokes simulation – (——) isothermal BC and (– –) adiabatic BC. The results from the numerical simulations in figure 16(*b*) have been adjusted by a factor $C < 1$ in such a way that $|\hat{p}_1|$ from both types of BC match the LST amplified mode for $y \gtrapprox 0.3$, respectively. $R_x = 1400$ (*a*) and 1500 (*b*).

Eissler & Bestek (1996) independently support Ma & Zhong (2003*a*)'s findings and our hypothesis. In their numerical simulation the beating, caused by a mode 1–2, remains visible longer than one would have expected from LST (see their figure 8). A longer lasting beat can be expected if the damping is weaker than predicted by LST. Our approach of comparing numerical amplitude functions with eigenfunctions from two different modes may be regarded as a simple qualitative analogue to the multi-mode decomposition of Tumin *et al.* (2007). It is understood that with such a decomposition, a more quantitative result will be achievable. However, we believe that our simple approach provides sufficient evidence to understand the flow dynamics, especially since we have used growth rates and phase velocities in addition to the pressure-amplitude functions.

In summary, the roughness is the source of an additional but stable disturbance, and the interaction of this disturbance with the unstable one causes a beat due to interference. The beating is more pronounced for an adiabatic boundary condition due to a smaller amplification and hence smaller absolute amplitude of the unstable mode (figure 13*b*). The role of the stable mode is further discussed in § 4.3.5.

4.3.3. *Disturbance evolution far behind the roughness*

Far downstream, the base flow and disturbance evolution return to a flat-plate behaviour again (figure 17). For $F = 1.0 \times 10^{-4}$ with a roughness element, the amplitude levels far downstream are considerably higher than in the flat-plate case (figure 17*a*). However, the calculation with a higher frequency, $F = 1.5 \times 10^{-4}$, shows that the far-downstream amplitude can be reduced significantly by the roughness (figure 17*b*). This effect is due to the region of the second-type instability being shifted to lower frequencies so that the amplification rate, for instance, in the range $1150 < R_x < 1200$, remains below the value for the flat plate. The shift shortens the streamwise region in which the second-type instability is active. Along the roughness, the disturbance is even further damped. In the case of the lower frequency, $F = 0.5 \times 10^{-4}$, the additional amplification and damping caused by the roughness are

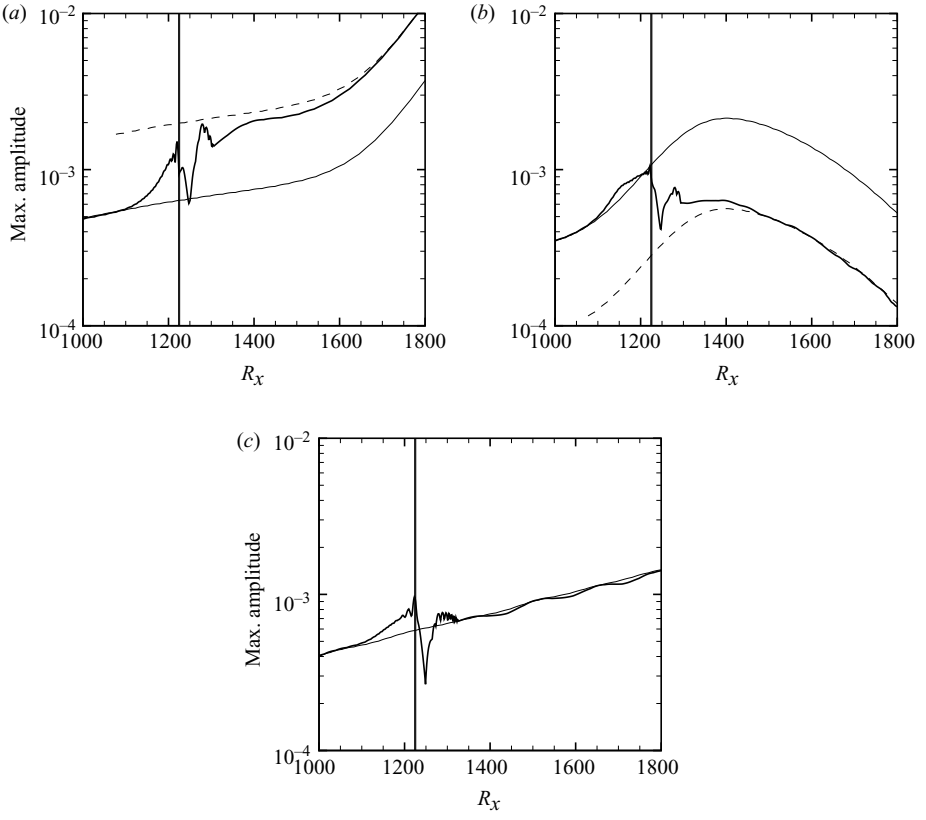

FIGURE 17. Streamwise evolution of maximum disturbance density $\hat{\rho}_1^{max}$ with (——) and without (——) roughness element, isothermal BC. The roughness element is centred at x=15 (R_x=1225) and has $h_R = 0.1$ and $l_R = 0.4$. Flat-plate results multiplied by a constant factor are also given (– –). (*a*) $F = 1.0 \times 10^{-4}$. (*b*) $F = 1.5 \times 10^{-4}$. (*c*) $F = 0.5 \times 10^{-4}$.

balanced (figure 17*c*) so that the obstacle does not introduce any significant (far-downstream) modification with respect to the smooth plate behaviour.

Overall, these results support the hypothesis that the roughness elements behave as disturbance amplifiers with a limited bandwidth, capable of filtering a range of frequencies and strongly amplify only a selected range. This range of unstable frequencies is narrower than that for the flat plate.

The high-frequency result ($F = 1.5 \times 10^{-4}$) does not exhibit a notable beat downstream of the roughness (figure 17*b*). This observation is in agreement with Eissler & Bestek (1996), who did not observe the excitation of a beat by blowing/suction in the region of the second-type instability.

4.3.4. *Influence of the roughness height*

An increase of disturbance amplitude can be seen not only in front of the roughness as discussed in §4.2.3, but also far downstream (figure 18). However, for small roughness heights $h \leqslant 0.05$ the increase in amplitude is more pronounced in front of the roughness than far downstream. This effect is stronger for a near-wall maximum (as it occurs for the streamwise velocity, figure 18*b*) than for a wall-distant maximum (as it occurs for the density, figure 18*a*). It is consistent with the observation that

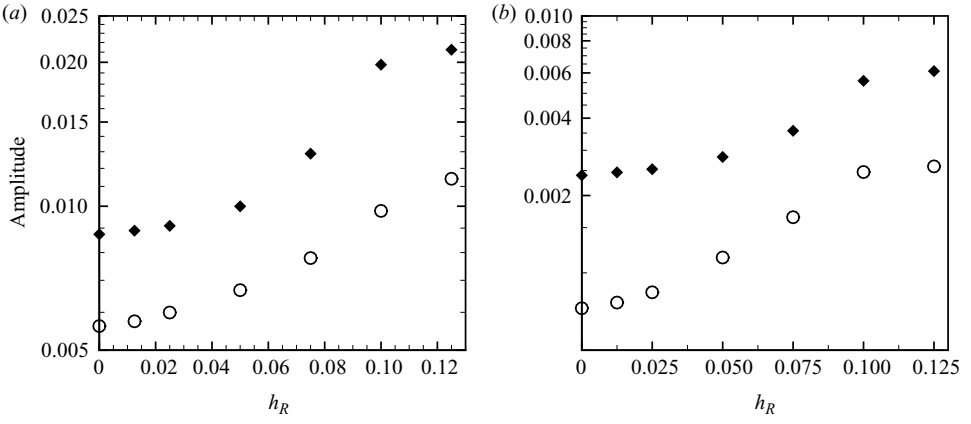

FIGURE 18. Maximum disturbance quantity $\hat{s}_1^{max}$ at $R_x = 1200$ (○) and $R_x = 1680$ (◆) vs. height of the roughness element with $l_R = 0.4$, adiabatic BC. (*a*) Density $\hat{\rho}_1^{max}$. (*b*) Streamwise velocity $\hat{u}_1^{max}$.

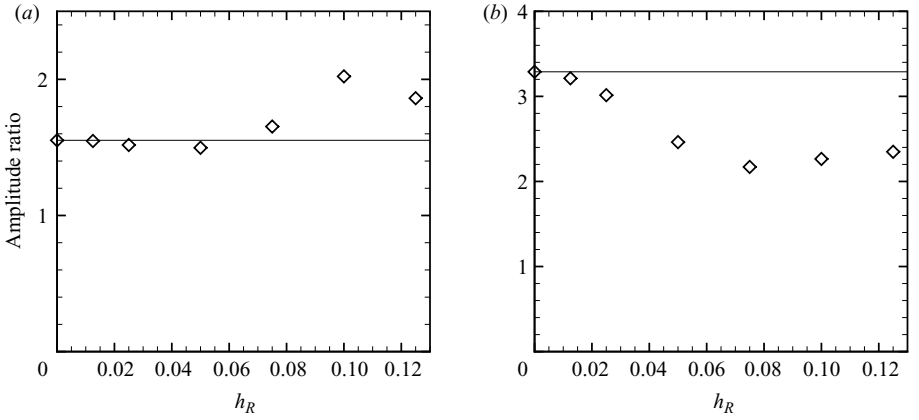

FIGURE 19. Ratio $\hat{s}_1^{max}(R_x = 1680)/\hat{s}_1^{max}(R_x = 1200)$ vs. height of the roughness element with $l_R = 0.4$, adiabatic BC. The horizontal lines mark the ratio observed for the flat plate $h_R \equiv 0$. (*a*) Density $\hat{\rho}_1^{max}$. (*b*) Streamwise velocity $\hat{u}_1^{max}$.

near-wall quantities are more strongly affected upstream of the roughness (see figure 7), i.e. it is regarded as a non-parallel effect.

The ratio of disturbance amplitude far downstream and immediately in front of the roughness, i.e. the quantity $\hat{s}_1^{max}(R_x = 1680)/\hat{s}_1^{max}(R_x = 1200)$, decreases slightly with increasing roughness height for $h \leqslant 0.05$ (figure 19). To understand this observation, we recall that along the roughness a region of damping occurs (see § 4.4.1) and this may explain why the relative amplitude gain (as compared with the flat plate $h_R \equiv 0$) far behind the roughness is smaller than in front of it.

For larger roughness heights ($h_R > 0.05$), however, the influence of the damping region is much less pronounced. For the density, the ratio of disturbance amplitudes far downstream and immediately in front of the roughness even becomes significantly larger than that for the flat plate (figure 19*a*). Hence, for a larger roughness an additional boost in amplitude occurs. For the streamwise velocity, the ratio still

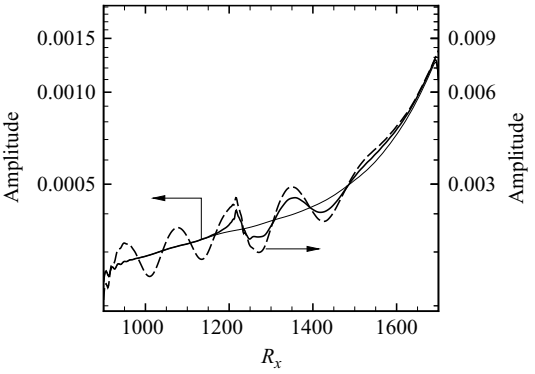

FIGURE 20. Maximum disturbance of the streamwise velocity $\hat{u}_1^{max}$, adiabatic boundary condition, for $F = 1.0 \times 10^{-4}$ and $h_R = 0.0125$, $l_R = 0.4$ for two different methods of disturbance forcing: original disturbance strip according to table 2 (——) and shortened strip (– –). Flat-plate results are given for reference (thin solid line).

remains smaller (figure 19*b*) due to the strong non-parallel effect in front of the roughness, but the ratio is at least seen to increase with roughness height for $h_R > 0.05$.

4.3.5. *Role of the stable mode*

A closer inspection is warranted to clarify whether the boost effect observed in the last section originates in the vicinity of the roughness or farther behind it. We concentrate on the region farther behind the roughness, while the next section (§ 4.4) is devoted to the vicinity of the roughness. Roughly, at $R_x \approx 1550$–1600 (for $F = 1.0 \times 10^{-4}$), the instability mechanism changes from the first to the second type. In the absence of the stable mode, the unstable mode (as identified in § 4.3.1) could be amplified due to both instability types, consecutively in x, as it happens in the case of the flat plate without roughness. Therefore, the only mechanism to explain an amplitude boost (beyond what happens for the flat plate) originating *farther behind* the roughness would be that the conversion-type mechanism of Fedorov & Khokhlov (2001) may be active. In this case, the stable mode 1–2 also contained in the signal should trigger the unstable mode and could be responsible for the amplitude boost.

To check if this conversion mechanism occurs here, a simulation with a shortened disturbance strip was carried out. As a result of the alteration, a beat is visible already upstream of the roughness (figure 20). The shortened disturbance strip possesses a different receptivity, so that the instability mode contained in the signal has a lower amplitude. To account for this change in amplitude and allow for a meaningful comparison with the results for the original disturbance strip, the scaling of the ordinate was adjusted (note the two different ordinates in figure 20). This was done in the following way: the scaling factor for the adjustment was selected such that both the dashed and the solid thick lines in figure 20 cross the flat-plate (thin solid) line at approximately the same streamwise locations in the interval $R_x \in [1200, 1500]$ behind the roughness, namely at $Re_x = 1232, 1306, 1393$ and 1485. Note that this interval lies before the expected conversion location. The same relative scaling between the simulations with the different disturbance strips has also been used in figure 23. The beat observed downstream of the roughness with the shorter strip is more pronounced as compared with the case with the original disturbance strip. However, far downstream (i.e. for $R_x > 1650$) no difference in the evolution of the unstable mode is visible when we compare the results from the two different forcing strips.

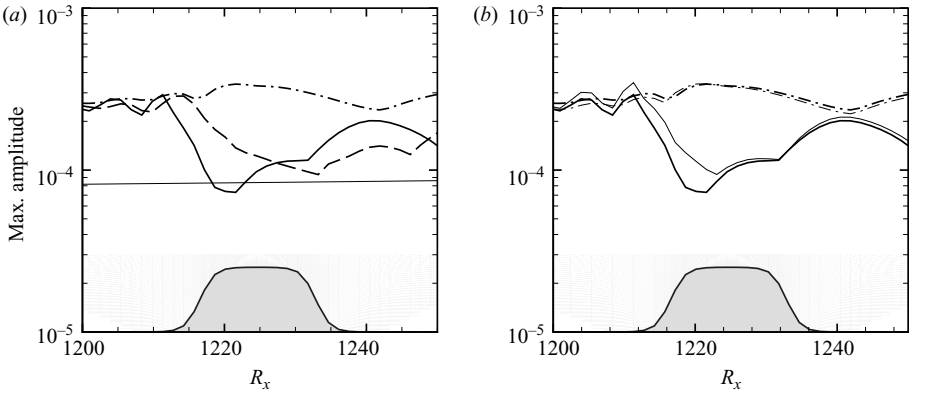

FIGURE 21. Streamwise evolution of the maximum amplitude in the Navier–Stokes simulation for $F = 1.0 \times 10^{-4}$: temperature $0.1 \times \hat{T}_1^{max}$ (–·–·–), streamwise velocity $\hat{u}_1^{max}$ (——), wall-normal velocity $\hat{v}_1^{max}$ (– –). The roughness with $h_R = 0.1$ and $l_R = 0.4$ is depicted in the figure (wall-normal extent not to scale). (*a*) Roughness (thick lines) vs. flat plate (thin line) for an isothermal BC. (*b*) Isothermal (thick lines) vs. adiabatic (thin lines) BC.

This suggests that a conversion did not take place, and the stable mode causes only transient growth. The additional boost in amplitude therefore originates most likely in the vicinity of the roughness, and this possibility shall be explored in §§ 4.4.2 and 4.4.3.

4.4. *Disturbance evolution in the vicinity of and along the roughness*

4.4.1. *Forward facing side and top of the roughness*

In the immediate vicinity upstream of and along the forward facing side of the roughness, the disturbance evolution is governed by rapid changes in both base flow and disturbance amplitude functions. In particular, the strong decrease in maximum amplitude in the range $R_x = [1200, 1220]$ visible for $\hat{u}_1$ or $\hat{v}_1$ (figure 21*a*) but not for $\hat{T}_1$ (again, figure 21*a*) is due to a strong change in amplitude functions. The amplification is quite similar for both temperature boundary conditions used here (figure 21*b*).

While the maximum for $\hat{u}_1$ is located close to the wall at $R_x = 1200$ (figure 22*a*), this near-wall maximum shrinks considerably so that the overall maximum is located away from the wall at $R_x = 1220$ (figure 22*b*). In contrast, for $\hat{T}_1$ it remains away from the wall the entire way (not shown). While amplitude functions for isothermal and adiabatic wall are almost identical at $R_x = 1200$, significant differences are visible near the wall at $R_x = 1220$.

Such a rapid change suggests that it may not be meaningful to analyse the flow in this region by considering only local profiles at a fixed location x. Therefore, no attempt is made to compare numerical results with local LST.

For all investigated frequencies ($F = 0.5, 1, 1.5 \times 10^{-4}$), the disturbance amplitudes are seen to decrease along the roughness (figure 17), although not simultaneously for all components (figure 21). The increased amplification observed upstream of the roughness is, hence, indeed counteracted by the damping along the roughness (as discussed in § 4.3.4).

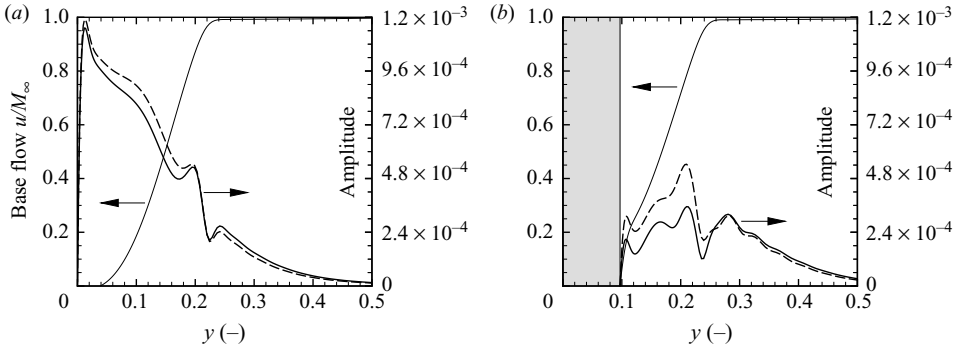

FIGURE 22. Wall-normal amplitude functions $|\hat{u}_1|$ for the forcing frequency $F = 1.0 \times 10^{-4}$ for an isothermal (——) and adiabatic (– –) boundary condition for the disturbance, roughness with $h_R = 0.1$ and $l_R = 0.4$. The base-flow profile (streamwise velocity) is given for reference. (*a*) $R_x = 1200$. (*b*) $R_x = 1220$.

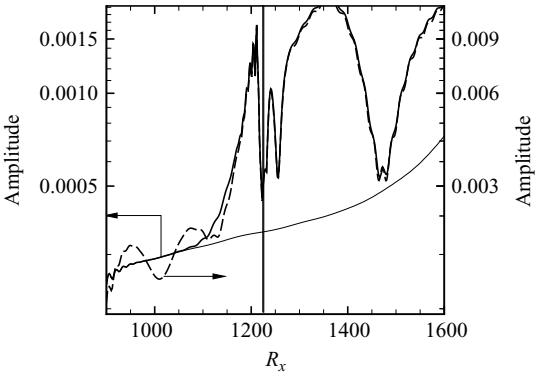

FIGURE 23. Maximum disturbance of the streamwise velocity $\hat{u}_1^{max}$, adiabatic boundary condition, for $F = 1.0 \times 10^{-4}$ and $h_R = 0.1$, $l_R = 0.4$, for two different methods of disturbance forcing. Flat-plate results are given for reference (thin line). The scaling for the simulations with roughness and the line legend are identical to the ones in figure 20.

4.4.2. *Backward facing side of the roughness*

Immediately downstream of the roughness, we see a rapid change in amplitude similar to the one along the forward facing side. The peak $\hat{u}$-amplitude directly behind the roughness occurs, again, inside the separation region in the same way as observed immediately upstream of it (as, e.g., plotted in figure 22*a*).

The discussion in § 4.3.2 has revealed that the roughness and its adjacent flow field are the source of an additional disturbance, mode 1–2. To demonstrate that the stable mode 1–2 originates mostly (if not exclusively) in the region behind and close to the roughness, the simulation with the altered disturbance strip has been repeated for a higher roughness. Results show that the evolution behind the roughness is independent of the stable mode 1–2 present upstream (figure 23). This observation can only be explained if the mode 1–2 from upstream does not experience a boost in amplitude, as otherwise a similar result as for the smaller roughness (figure 20) must have been observable. It can be regarded as evidence that the stable mode 1–2 behind the roughness indeed originates at the roughness.

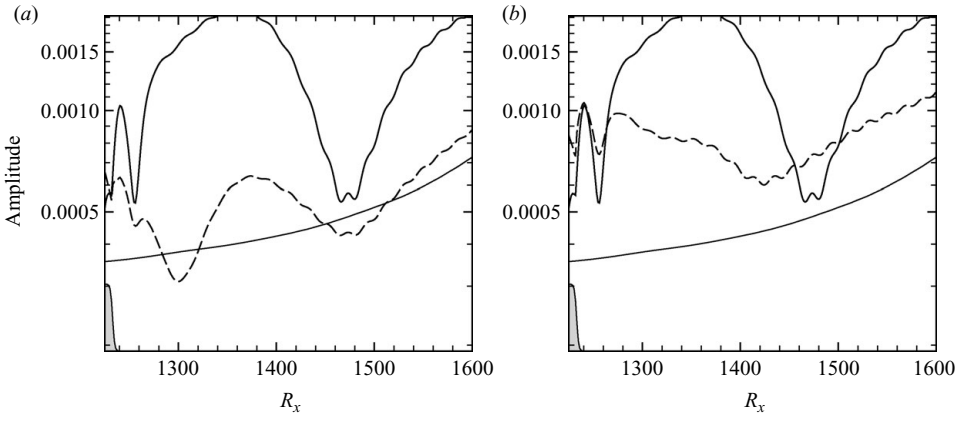

FIGURE 24. Maximum disturbance of the streamwise velocity $\hat{u}_1^{max}$, adiabatic boundary condition, for $F = 1.0 \times 10^{-4}$ for $l_R = 0.4$ and two different roughness heights h_R, respectively. Flat-plate results are given for reference (thin line). (*a*) $h_R = 0.05$ (– –) and $h_R = 0.1$ (——). (*b*) $h_R = 0.075$ (– –) and $h_R = 0.1$ (——).

Downstream of the rear separation region the two roughness heights $h_R = 0.05$ and $h_R = 0.1$ exhibit the opposite disturbance evolution (figure 24*a*): while the disturbance amplitude strongly increases for $h_R = 0.1$, it decreases at first for $h_R = 0.05$. All cases $h_R \leqslant 0.05$ have the same qualitative behaviour (see also figure 20), i.e. the decreasing amplitude. Heights $h_R = 0.1$ and $h_R = 0.125$, on the other hand, exhibit the increasing behaviour. Interestingly, for the case with $h_R = 0.075$, only a very weak beating can be observed (figure 24*b*). Our results, therefore, suggest that the phase difference between the stable and the unstable modes depends on the height of the roughness.

We finally note that the strength of the beating, and therefore the amplitude of the stable mode 1–2, changes with roughness height (compare all the thick lines in figures 20 and 24*a*). Similarly, the distance between locations of destructive interference changes with the height (again, see figures 20 and 24*a*). This can be explained by a height-dependent difference in phase speed between the stable mode 1–2 and the instability mode.

4.4.3. *Discussion*

In § 4.3.5 we have evaluated the role of the stable mode, and in § 4.4.2 we have discussed the location of its origin. Now, the generation mechanism of the stable mode 1–2 and the amplitude boost of the instability mode warrant a closer inspection. Two different possibilities regarding the respective generation mechanisms and interconnections between the disturbance modes are, therefore, discussed below.

One possibility for the generation of the stable mode 1–2 is an inversion of the conversion mechanism of Fedorov & Khokhlov (2001). According to such a mechanism, the conversion of a stable mode to an instability mode should take place around the streamwise location where eigenvalues come closest in the complex plane. This point is usually not far away from the point of matching phase velocities. Here, the inverse conversion from the unstable mode immediately behind the roughness to the stable mode farther downstream could occur. If we assume that that such a conversion has taken place for instance for $F = 1.0 \times 10^{-4}$ and $h_R = 0.1$, it must have occurred upstream of $R_x = 1300$, as the phase velocities of both the stable and the unstable modes diverge downstream of the roughness (figure 15*b*; $R_x < 1350$).

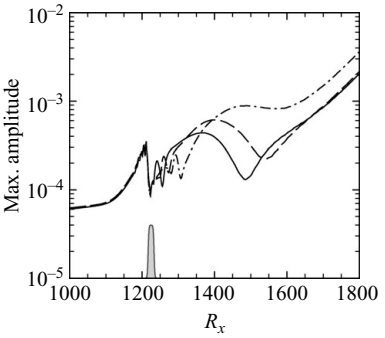

FIGURE 25. Streamwise evolution of $\hat{u_1}^{max}$ in Navier–Stokes simulations with forcing at $F = 1.0 \times 10^{-4}$ and $h_R = 0.1$. Results are for length $l_R = 0.4$ (——), $l_R = 0.8$ (– –), $l_R = 1.6$ (- · - ·). The roughness with $l_R = 0.4$ is shown as grey contour (height not to scale).

A drawback of this interpretation is that it cannot easily explain the dependence of the strength of the beat on the height of the roughness: if the stable mode 1–2 is directly caused by the instability mode, the amplitude of the stable mode should depend on the amplitude of the generating mode. In other words, the relation of the amplitude of the instability mode and the stable mode should remain roughly the same. Instead, for a small roughness the beat is weak and, hence, the amplitude of the stable mode 1–2 is much smaller than that of the instability mode, while for the larger roughness the beat is strong, which means that both the stable and the instability modes possess a similarly large amplitude. Moreover, we did not even observe the regular conversion mechanism (from stable to unstable modes) to take place far behind the roughness as detailed in § 4.3.2, which makes it an unlikely process to occur.

Another possibility is that both the stable mode 1–2 and the instability mode are triggered or strongly influenced by the shock. Significant fluctuations, of the order of the boundary-layer perturbations, were found to occur along the oblique shock behind the roughness. The origin of the perturbation of the oblique shock is probably the density: the density perturbation at the edge of the boundary layer connects to the shock and may cause it to oscillate. These oscillations are also visible in the pressure. Interestingly, for a three-dimensional roughness element, Tumin (2006) found that perturbations have large amplitudes along the Mach waves caused by the roughness.

The pressure perturbations in the free stream may, in turn, excite both the stable mode 1–2 and the instability mode, with the latter effect leading to an amplitude boost. We note that Ma & Zhong (2003*b*) argued that free-stream perturbations can excite instability modes. As the strength of the shock depends on the height of the roughness, a height dependence can be expected. As further evidence that the shock is involved, simulations with different lengths of the roughness exhibited a larger resulting far-downstream amplitude for the longer roughness (figure 25), which we find unlikely to be explained only by the slightly larger separation regions (see figure 4*b*). Instead, the differences in angle between the shock and local streamline for the three cases may be responsible. However, further investigations are required to clarify this.

5. Conclusions

Results from Navier–Stokes simulations of a flat-plate compressible boundary layer with a bar-type roughness element have been reported and analysed. In particular, the

alteration of the evolution of a convective boundary-layer disturbance by a localized two-dimensional roughness is discussed. Physical insight was gained with the aid of parameter variations such as height and length of the roughness, as well as disturbance frequency. The interpretation of simulation results was aided by a local linear stability analysis.

A separating boundary layer boosts the amplification of both first(inflectional)- and second(acoustic)-type instability mechanisms as a result of more convectively unstable boundary-layer profiles. This boost is concentrated at lower frequencies as the frequency-range of the second-type instability shifts towards lower values due to an increase in boundary-layer thickness. The overall maximum amplification rate is found within the region of adverse-pressure gradient upstream of the roughness, and the instability in front of the roughness is independent of the (downstream) length of the roughness. The lower the roughness height the weaker an effect on the instability, in terms of both the spatial expansion and the maximum amplification rate.

Within the region of the first-type instability, numerical results of two-dimensional instability waves exhibit a very good agreement with LST in both amplitude functions and phase velocities even in regions of increasingly non-parallel flow, while amplification rates are systematically underpredicted. Within the second-type instability region, a good matching of amplification rates is observed, while deviations in amplitude functions are visible and phase velocities are underpredicted by LST. The Navier–Stokes simulations reveal that the stabilization observed in LST for two-dimensional first-type instability modes is due to deficiencies in the theory likely caused by non-parallel effects. Hence, LST predicts an incorrect trend (stabilization instead of destabilization) for two-dimensional modes with first-type instability characteristics. The trend for oblique (three-dimensional) modes (a destabilization) is predicted correctly.

Downstream of the roughness, an additional disturbance is generated and interacts with the one coming from upstream. As a result, the disturbance signal behind the roughness exhibits a beating: constructive (and destructive) interference occurs. The additional disturbance is a stable mode 1–2, which possesses a similar phase velocity as the unstable mode in the vicinity of the roughness. The stable mode could be identified based on the amplitude function associated with this stable mode, as it possesses notable values at the wall only. Therefore, we did not feel the need to apply a multi-mode decomposition as proposed by Tumin (2007). The shape of the amplitude function also explains why we could clearly observe the instability mode away from the wall in spite of the beat. Far downstream, the amplification rate of a flat plate for the same distance from the leading edge is recovered. The stable mode appears to cause only transient growth, as we did not find evidence that a conversion to the instability wave takes place.

Along the roughness, the disturbance is always found to be strongly damped. Because of this damping, the net effect for disturbances at low frequencies turns out to be zero despite an increased amplification upstream of the roughness. At high frequencies (second-type instability even without roughness), the net effect is even strongly negative, i.e. the far downstream amplitude is significantly smaller than for a flat plate. Only for frequencies that lie in the first-type instability region if no roughness is present, but are amplified due to a second-type mechanisms in the vicinity of the roughness, a gain in amplitude over the flat-plate case is observed. Hence, a two-dimensional roughness element behaves as a disturbance amplifier with a limited bandwidth, capable of filtering a range of frequencies and strongly amplifying only a selected range.

The generation mechanism of the stable and an amplitude boost of the unstable mode have been discussed, and this mechanism seems to be active in the rear of the roughness. These interactions certainly warrant further investigations.

Financial support from NASA under contract no. NNX07AC29A is gratefully acknowledged. We are grateful to S. Lele and A. Mani, Stanford University, for useful discussions and for providing the simulation code.

REFERENCES

Anderson, J. D. 2000 *Hypersonic and High Temperature Gas Dynamics*. AIAA.

Balakumar, P. 2003 Transition in a supersonic boundary-layer due to roughness and acoustic disturbances. *Paper*, 2003-3589. AIAA.

Balakumar, P. & Malik, M. R. 1992 Discrete modes and continuous spectra in supersonic boundary layers. *J. Fluid Mech.* **239**, 631–656.

Eissler, W. & Bestek, H. 1996 Spatial numerical simulations of linear and weakly nonlinear wave instabilities in supersonic boundary layers. *Theoret. Comput. Fluid Dyn.* **8** (3), 219–235.

Fedorov, A. V. 2003 Receptivity of a high-speed boundary layer to acoustic disturbances. *J. Fluid Mech.* **491**, 101–129.

Fedorov, A. V. & Khokhlov, A. P. 1993 Excitation and evolution of unstable disturbances in supersonic boundary layer. In *Transitional and Turbulent Compressible Flows* (ed. L. D. Kral & T. A. Zang), vol. 151, pp. 1–13. ASME.

Fedorov, A. V. & Khokhlov, A. P. 2001 Prehistory of instability in a hypersonic boundary layer. *Theor. Comp. Fluid Dyn.* **14**, 359–375.

Fezer, A. & Kloker, M. 2002 DNS of transition mechanisms at Mach 6.8—flat plate vs. sharp cone. In *West East High Speed Flow Fields 2002* (ed. D. E. Zeitoun, J. Periaux, J. A. Désidéri & M. Marini), pp. 1–8. CIMNE.

Herbert, T. 1997 Parabolized stability equations. *Ann. Rev. Fluid Mech.* **29**, 245–283.

Ma, Y. & Zhong, X. 2003*a* Receptivity of a supersonic boundary layer over a flat plate. Part 1. Wave structures and interactions. *J. Fluid Mech.* **488**, 31–78.

Ma, Y. & Zhong, X. 2003*b* Receptivity of a supersonic boundary layer over a flat plate. Part 2. Receptivity to free-stream sound. *J. Fluid Mech.* **488**, 79–121.

Mack, L. M. 1969 Boundary layer stability theory. *Tech. Rep.* JPL-900-277-REV-A; NASA-CR-131501. Jet Propulsion Laboratory, NASA.

Mack, L. M. 1975 Linear stability theory and the problem of supersonic boundary-layer transition. *AIAA J.* **13** (3), 278–2285.

Malik, M. R. 1989 Prediction and control of transition in supersonic and hypersonic boundary layers. *AIAA J.* **27** (11), 1487–1493.

Malik, M. R. 2003 Hypersonic flight transition data analysis using parabolized stability equations with chemistry effects. *J. Spacecraft Rockets* **40** (3), 332–344.

Malik, M. R. & Anderson, E. C. 1991 Real gas effects on hypersonic boundary-layer stability. *Phys. Fluids* A **3** (5), 803–821.

Marxen, O. & Iaccarino, G. 2008*a* An immersed boundary method for numerical simulations of high-speed boundary layers with two- and three-dimensional roughness. In *Annual Research Briefs 2008*, pp. 89–100. Center for Turbulence Research, Stanford University.

Marxen, O. & Iaccarino, G. 2008*b* Numerical simulation of the effect of a roughness element on high-speed boundary-layer instability. *Paper* 2008-4400. AIAA.

Marxen, O., Iaccarino, G. & Shaqfeh, E. S. G. 2007 Numerical simulation of hypersonic instability using different gas models. In *Annual Research Briefs 2007*, pp. 15–27. Center for Turbulence Research, Stanford University.

Nagarajan, S., Lele, S. K. & Ferziger, J. H. 2003 A robust high-order method for large eddy simulation. *J. Comput. Phys.* **191**, 392–419.

Nagarajan, S., Lele, S. K. & Ferziger, J. H. 2007 Leading-edge effects in bypass transition. *J. Fluid Mech.* **572**, 471–504.

Pagella, A., Babucke, A. & Rist, U. 2004 Two-dimensional numerical investigations of small-amplitude disturbances in a boundary layer at $Ma = 4.8$: compression corner versus impinging shock wave. *Phys. Fluids* **16** (7), 2272–2281.

Pagella, A., Rist, U. & Wagner, S. 2002 Numerical investigations of small-amplitude disturbances in a boundary layer with impinging shock wave at $Ma = 4.8$. *Phys. Fluids* **14** (7), 2088–2100.

Robinet, J. C. 2007 Bifurcations in shock-wave/laminar–boundary-layer interaction: global instability approach. *J. Fluid Mech.* **579**, 85–112.

Schmid, P. J. & Henningson, D. S. 2001 *Stability and Transition in Shear Flows*, 1st ed. Springer.

Sipp, D. & Lebedev, A. 2007 Global stability of base and mean flows: a general approach and its applications to cylinder and open cavity flows. *J. Fluid Mech.* **593**, 333–358.

Tumin, A. 2006 Receptivity of compressible boundary layers to three-dimensional wall perturbations. *Paper* 2006-1110. AIAA.

Tumin, A. 2007 Three-dimensional spatial normal modes in compressible boundary layers. *J. Fluid Mech.* **586**, 295–322.

Tumin, A. & Reshotko, E. 2005 Receptivity of a boundary-layer flow to a three-dimensional hump at finite Reynolds numbers. *Phys. Fluids* **17**, 094101.

Tumin, A., Wang, X. & Zhong, X. 2007 Direct numerical simulation and the theory of receptivity in a hypersonic boundary layer. *Phys. Fluids* **19**, 014101.